

A MODEL FOR ANISOTROPIC INTERSTELLAR SCATTERING AND ITS APPLICATION TO SGR A*

DIMITRIOS PSALTIS,^{1,2,3} MICHAEL D. JOHNSON,^{4,3} RAMESH NARAYAN,^{4,3} LIA MEDEIROS,^{1,5} LINDY BLACKBURN,⁴ AND
GEOFF C. BOWER⁶

¹*Astronomy Department, University of Arizona, 933 N. Cherry Ave, Tucson, AZ 85721*

²*Radcliffe Institute for Advanced Study, Harvard University, Cambridge, MA 02138, USA*

³*Black Hole Initiative, Harvard University, 20 Garden St., Cambridge, MA 02138*

⁴*Harvard-Smithsonian Center for Astrophysics, 60 Garden Street, Cambridge, MA 02138, USA*

⁵*Department of Physics, Broida Hall, University of California Santa Barbara, Santa Barbara, CA 93106*

⁶*Academia Sinica Institute of Astronomy and Astrophysics, 645 N. A'ohoku Place, Hilo, HI 96720, USA*

ABSTRACT

Scattering in the ionized interstellar medium is commonly observed to be anisotropic, with theories of magnetohydrodynamic (MHD) turbulence explaining the anisotropy through a preferred magnetic field direction throughout the scattering regions. In particular, the line of sight to the Galactic Center supermassive black hole, Sgr A*, exhibits strong and anisotropic scattering, which dominates its observed size at wavelengths of a few millimeters and longer. Therefore, inferences of the intrinsic structure of Sgr A* at these wavelengths are sensitive to the assumed scattering model. In addition, extrapolations of the scattering model from long wavelengths, at which its parameters are usually estimated, to 1.3 mm, where the Event Horizon Telescope (EHT) seeks to image Sgr A* on Schwarzschild-radius scales, are also sensitive to the assumed scattering model. Past studies of Sgr A* have relied on simple Gaussian models for the scattering kernel that effectively presume an inner scale of turbulence far greater than the diffractive scale; this assumption is likely violated for Sgr A* at 1.3 mm. We develop a physically motivated model for anisotropic scattering, using a simplified model for MHD turbulence with a finite inner scale and a wandering transverse magnetic field direction. We explore several explicit analytic models for this wandering and derive the expected observational properties — scatter broadening and refractive scintillation — for each. For expected values of the inner scale, the scattering kernel for all models is markedly non-Gaussian at 1.3 mm but is straightforward to calculate and depends only weakly on the assumed model for the wandering of the magnetic field direction. On the other hand, in all models, the refractive substructure depends strongly on the wandering model and may be an important consideration in imaging Sgr A* with the EHT.

Keywords: radio continuum: ISM – scattering – ISM: structure – Galaxy: nucleus – techniques: interferometric
— turbulence

1. INTRODUCTION

The supermassive black hole, Sgr A*, at the center of the Milky Way lies behind one or more scattering “screens” that affect the observational appearance of the black hole at radio wavelengths. Within these scattering regions, small-scale fluctuations in the density of free electrons introduce stochastic phase variations in electromagnetic waves traveling along different paths from the Galactic Center to the Earth. These phase variations lead to a number of astrometric, timing, and spectral effects (see [Rickett 1990](#); [Narayan 1992](#), for reviews of scattering effects), the most important of which, in the case of Sgr A*, is the broadening of the source image at millimeter and longer wavelengths.

The properties of the scattering towards Sgr A* have been explored observationally via measurements of the wavelength dependence of its scatter-broadened image (see, e.g., [Lo et al. 1993, 1998](#); [Krichbaum et al. 1998](#); [Bower et al. 2004](#); [Shen et al. 2005](#); [Bower et al. 2006](#); [Lu et al. 2011](#); [Bower et al. 2014b](#); [Ortiz-León et al. 2016](#)), via observations of the images of nearby OH masers and of the free-free emission and absorption properties of the screen ([van Langevelde et al. 1992](#); [Frail et al. 1994](#); [Lazio & Cordes 1998a,b](#)), as well as via measurements of the temporal and angular broadening of the Galactic Center magnetar ([Spitler et al. 2014](#); [Bower et al. 2014a](#)). All these observations have shown that scattering towards Sgr A* is highly anisotropic, with a major-to-minor axis ratio for the ensemble average scattering kernel of ~ 2 . Recently, [Gwinn et al. \(2014\)](#) discovered refractive substructure in very long baseline interferometry (VLBI) observations of Sgr A* at 1.3 cm, demonstrating that, at this wavelength, scatter-broadening occurs in the “Average” regime (see Table 1). The location of the scattering screen was originally inferred based on the scatter broadening of background sources, which place the screen close to the Galactic Center ([Lazio & Cordes 1998b](#)). More recent inferences based on the Galactic Center magnetar place it closer to Earth, possibly in an intervening spiral arm ([Bower et al. 2014a](#)). Observations of scattering effects in pulsars in the direction of the Galactic Center offered hints for a more complex configuration with multiple screens at various distances ([Dexter et al. 2017](#)).

Early mm observations (see, e.g., [Krichbaum et al. 1998](#); [Doeleman et al. 2001](#)), as well as theoretical expectations of the wavelength dependence of the image size of the accretion flow around Sgr A* ([Özel et al. 2000](#); [Falcke et al. 2000](#)), strongly suggested that, at mm-wavelengths, the effects of scattering would be minimal. Indeed, VLBI observations with a small number of baselines have since demonstrated that the image of Sgr A* at 1.3 mm has a size comparable to the expected size of the black hole shadow ([Doeleman et al. 2008](#); [Fish et al. 2011](#); [Johnson et al. 2015](#)) and that it has asymmetric intrinsic structure ([Fish et al. 2016](#)). At this wavelength, the inferred source size of $\sim 40 \mu\text{as}$ is significantly larger than the expected scatter broadening (roughly $20 \mu\text{as} \times 10 \mu\text{as}$). Therefore, direct observations of the shadow that the black hole casts on the surrounding ac-

cretion disk emission ([Bardeen 1973](#); [Luminet 1979](#); [Falcke et al. 2000](#)) should be feasible and will only be modestly affected by the scattering.

In April 2017, the Event Horizon Telescope (EHT), which is a mm-VLBI array with stations from Hawaii to France and from Arizona to the South Pole, performed the first full-array interferometric observations of Sgr A* with the primary aim of obtaining images with horizon-scale resolution. Mitigating the effects of scattering on these images ([Fish et al. 2014](#); [Johnson 2016](#)), applying statistical tools to extract the parameters of the black hole shadow ([Psaltis et al. 2015](#)) or to compare the observed image to model predictions (see, e.g., [Broderick et al. 2009](#); [Dexter et al. 2009, 2010](#); [Mościbrodzka et al. 2009, 2014](#); [Kim et al. 2016](#)), all require a model for the effects of interstellar scattering at EHT wavelengths. The scattering parameters are typically constrained by observations at longer wavelengths (typically at $\gtrsim 1$ cm; see, e.g., [Bower et al. 2006](#)) and a scattering model is used to extrapolate them to EHT wavelengths.

The theory behind the effects of interstellar scattering on the images of astrophysical objects has been developed in a number of studies during the last four decades (see, e.g., [Cronyn 1972](#); [Cohen & Cronyn 1974](#); [Lee & Jokipii 1975a,b,c](#); [Blandford & Narayan 1985](#); [Goodman & Narayan 1985](#); [Narayan & Goodman 1989](#); [Goodman & Narayan 1989](#); [Johnson & Gwinn 2015](#); [Johnson & Narayan 2016](#)). While many of these studies considered isotropic scattering, [Narayan & Hubbard \(1988\)](#) developed a model for anisotropic scattering in planetary atmospheres based on a particular phenomenological model of the anisotropic power spectrum of the underlying density fluctuations; a few other previous studies (e.g., [Goodman & Narayan 1989](#); [Johnson & Gwinn 2015](#)) also implemented anisotropy in their discussions. [Chandran & Backer \(2002\)](#) studied the effects of interstellar scattering on images using an anisotropic Goldreich-Sridhar power spectrum for the turbulent fluctuations ([Goldreich & Sridhar 1995, 1997](#)) and derived a relation between the degree of anisotropy in the scattering kernel and of the wandering of the projected magnetic field vector along the line-of-sight.

In fitting data, especially in the case of Sgr A*, anisotropic scattering has generally been treated with simple empirical models, such as an anisotropic Gaussian scattering kernel with a wavelength-independent orientation and degree of anisotropy (this model was indeed used in all the observational studies mentioned earlier). The Gaussian model is adequate so long as the diffractive scale of scattering is much smaller than the inner scale of turbulence in the scattering screen. However, in the case of EHT observations, it is possible that the diffractive scale will become comparable to or even larger than the turbulence inner scale (see Figure 1 below). Our aim here is to bridge the gap between the empirical Gaussian kernel approach and more rigorous theoretical models for scattering. To this end, we develop a model of interstellar scattering along the line-of-sight towards Sgr A* that (i) is anisotropic, (ii) incorporates explicitly the effects of a finite inner scale, and (iii) has enough degrees of freedom

to model and interpret upcoming EHT data with appropriate uncertainties in the scattering model incorporated into the error budget.

2. THE SCATTERING SCREEN TOWARDS SGR A*

Under the usual assumption of a single, thin scattering screen between the Earth and Sgr A*, we can describe fully the statistical properties of the inhomogeneities that lead to scattering in terms of the phase structure function $D_\phi(\vec{r})$, where \vec{r} is a transverse 2-vector on the projected scattering screen. The phase structure function measures the second order correlation between the change in phase $\phi(\vec{r})$ introduced by the screen to the propagating radio waves at two different locations separated by a transverse distance \vec{r} , i.e.,

$$D_\phi(\vec{r}) \equiv \langle [\phi(\vec{r}_0 + \vec{r}) - \phi(\vec{r}_0)]^2 \rangle. \quad (1)$$

This function is related to the phase correlation function $C(\vec{r})$ by

$$D_\phi(\vec{r}) = 2[C(0) - C(\vec{r})], \quad (2)$$

and $C(\vec{r})$ is related to the power spectrum of fluctuations in the turbulent screen $Q(\vec{q})$ by

$$C(\vec{r}) = \frac{\lambda^2}{4\pi^2} \int Q(\vec{q}) \exp(i\vec{q} \cdot \vec{r}) d^2q. \quad (3)$$

Here $\lambda \equiv 2\pi\lambda$ is the wavelength of observations and \vec{q} is a transverse spatial frequency vector. As written, $D_\phi(\vec{r})$, $C(\vec{r})$ and $Q(\vec{q})$ are all dimensionless.

We define the diffractive scale r_{dif} as the transverse length on the scattering screen over which the phase structure function becomes equal to unity, i.e.,

$$D_\phi(r_{\text{dif}}) = 1. \quad (4)$$

The diffractive scale is related to the angular size of the scatter-broadened image of a point source θ_{scat} by

$$r_{\text{dif}} \simeq \frac{\sqrt{2\ln 2}}{\pi} \frac{\lambda}{(1+M)\theta_{\text{scat}}} \simeq 4.1 \times 10^7 \left(\frac{\lambda}{\text{cm}} \right)^{-1} \text{ cm}. \quad (5)$$

The diffractive scale depends on the overall scattering geometry, described using the magnification $M \equiv D/R$, where D is the distance between the screen and the observer, and R is the distance between the screen and the source. In this work, motivated by observations of Sgr A*, we take the scattering kernel to be anisotropic. Therefore, r_{dif} depends on orientation. In the last equality above, we used typical values of the wavelength-dependent image size of Sgr A* along the major axis of the scattering kernel, as observed at \sim cm wavelengths (see, e.g., Bower et al. 2006; Psaltis et al. 2015, and references therein), which lead to the approximation (assuming a Gaussian scattering kernel for simplicity)

$$\theta_{\text{scat}} \equiv \theta_{\text{SGRA}} \simeq 1.32 \left(\frac{\lambda}{\text{cm}} \right)^2 \text{ mas}. \quad (6)$$

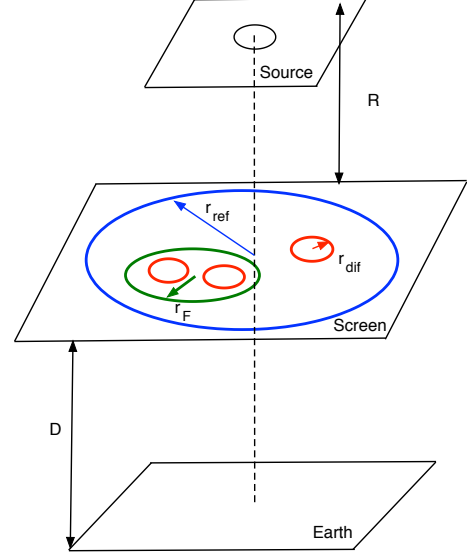


Figure 1. A schematic of the diffractive, Fresnel, and refractive scales, as well as a depiction of the definitions of the distances between the Earth, the scattering screen, and the source that we use in the text.

In addition to the diffractive scale, another scale of importance is the Fresnel scale,

$$r_{\text{F}} \equiv \left(\frac{DR}{D+R} \lambda \right)^{1/2} = \left(\frac{D\lambda}{1+M} \right)^{1/2}, \quad (7)$$

where $\lambda = \lambda/2\pi$ is the wavelength of observations.

In the strong scattering regime, defined as the regime where $r_{\text{dif}} \ll r_{\text{F}}$, a third important scale is the refractive scale,

$$r_{\text{ref}} \equiv \frac{r_{\text{F}}^2}{r_{\text{dif}}}, \quad (8)$$

which corresponds to the projected size of the image of a point source on the scattering screen, i.e.,

$$r_{\text{ref}} \simeq \frac{\theta_{\text{scat}} D}{2\sqrt{2\ln 2}} \simeq 2.3 \times 10^{13} \left(\frac{\lambda}{\text{cm}} \right)^2 \left(\frac{D}{2.7 \text{ kpc}} \right) \text{ cm}, \quad (9)$$

where we have used the distance to the screen as inferred from observations of the Galactic Center magnetar (Bower et al. 2014a). All three length scales, r_{dif} , r_{F} , r_{ref} , depend on wavelength.

Figures 1 and 2 show a schematic diagram and the sizes of the three characteristic scales for the scattering screen towards Sgr A* as a function of wavelength, respectively. The second figure also shows estimates of the inner scale of turbulence in the scattering screen towards Sgr A*, which range from $\simeq 50$ – 10^4 km (see, e.g., Spangler & Gwinn 1990; Rickett et al. 2009; Gwinn et al. 2014). At the ~ 3 – 20 cm wavelengths where measurements of the properties of the scattering screen towards Sgr A* are usually carried out, the inner scale of turbulence is larger than the diffractive scale, consistent with the measurement of a quadratic dependence of the

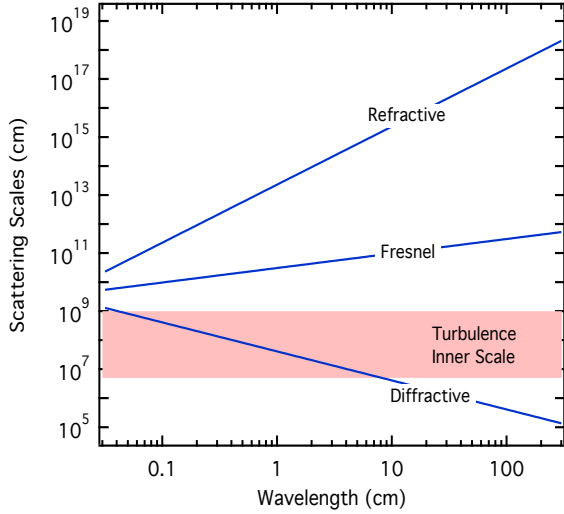


Figure 2. The diffractive, Fresnel, and refractive scales as a function of wavelength for the typical parameters of the screen towards Sgr A* and for the magnification set to zero. The horizontal shaded band shows the range of inner scale of turbulence, as inferred for the interstellar medium in general and for the screen towards Sgr A* in particular. At the \simeq mm wavelengths of the EHT, it is likely that the diffractive scale is comparable to or larger than the inner scale of turbulence.

scatter-broadened image size on wavelength (see, e.g., Bower et al. 2004, 2006). However, it is likely that the diffractive scale becomes larger than the inner scale of turbulence at the \simeq mm wavelengths of the EHT. As a result, extrapolating the properties of the scattering screen from a few cm to \simeq mm wavelengths requires taking explicitly into account the finite size of the inner scale of turbulence in the screen.

The various characteristic length scales allow us to define two corresponding timescales: the diffractive timescale

$$t_{\text{dif}} \equiv \frac{r_{\text{dif}}}{u} \simeq 8.2 \left(\frac{\lambda}{\text{cm}} \right)^{-1} \left(\frac{u}{50 \text{ km s}^{-1}} \right)^{-1} \text{ s}, \quad (10)$$

and the refractive timescale

$$t_{\text{ref}} \equiv \frac{r_{\text{ref}}}{u} \simeq 0.15 \left(\frac{\lambda}{\text{cm}} \right)^2 \left(\frac{D}{2.7 \text{ kpc}} \right) \left(\frac{u}{50 \text{ km s}^{-1}} \right)^{-1} \text{ yr}, \quad (11)$$

where u is the transverse relative velocity between the source, the screen, and the observer. Narayan & Goodman (1989) and Goodman & Narayan (1989) identified three regimes of scattering effects on interferometric imaging: the snapshot regime, the average regime, and the ensemble average regime (see above references for the exact definitions). The regime applicable in each case depends on the integration time t_{int} and the bandwidth $\delta\nu/\nu$ of the instrument used for the measurement of the interferometric visibilities, as well as on the source size (before scattering) θ_{src} . Table 1 summarizes the conditions for the three regimes (based on the work of Goodman & Narayan 1989) under the assumption that the charac-

teristic baseline length at a given wavelength is comparable to r_{dif} . For all wavelengths and instruments of interest, interferometric imaging of Sgr A* takes place in the average regime (see also Gwinn et al. 2014; Johnson & Gwinn 2015; Johnson & Narayan 2016; Johnson 2016).

3. MODELING THE SOURCE OF ANISOTROPY

Interstellar scattering is caused by electron density fluctuations along the line-of-sight, which are believed to be the result of turbulence in the magnetized interstellar medium. Models of MHD turbulence (Goldreich & Sridhar 1995) indicate that turbulent eddies are highly elongated along the local direction of the magnetic field. This anisotropy in density fluctuations should induce anisotropic scattering. As discussed in the introduction, high resolution observations of Sgr A* at cm wavelengths do reveal anisotropically scatter-broadened images, with major and minor axes in a two-to-one ratio. The scattering angles along the two axes scale as the square of the observing wavelength (see, e.g., Bower et al. 2004, 2006); a priori, this seems inconsistent with a turbulent spectrum of density fluctuations, which would predict a scaling proportional to $\lambda^{11/5}$ for a Kolmogorov-like turbulence spectrum (e.g., Goodman & Narayan 1985). However, a quadratic wavelength dependence would be consistent with expectations, if the inner scale of the turbulence is larger than the diffractive scale, as is expected to be the case at cm and longer wavelengths (Fig. 2). However, we expect r_{dif} to be comparable to the inner scale at the shorter (mm) wavelengths of the EHT, and hence there is a need to go beyond the usual λ^2 models of scattering.

Motivated by the above, we include the following features in our model of the phase structure function $D_\phi(\vec{r})$ and its corresponding power spectrum $Q(\vec{q})$:

(i) The power spectrum has a power-law form $\propto q^{-(\alpha+2)}$, where the index α is a free parameter but is expected to be close to the Kolmogorov value $\alpha = 5/3$.

(ii) The power spectrum has an inner scale, which we will call r_{in} .

(iii) The scattering is anisotropic, reflecting the presence of a preferred direction of the projected magnetic field.

(iv) The strength of the scattering and the degree and orientation of its anisotropy vary with depth in the scattering screen. To accommodate this, we decompose the screen into a superposition of independent layers along the line-of-sight (though still within a single thin screen approximation).

(v) Within any given layer in the screen, we assume infinite anisotropy of the relevant turbulent eddies. According to the Goldreich & Sridhar (1995) theory of MHD turbulence, anisotropic eddies on a given scale r have an axis ratio $\sim (r/L_{\text{out}})^{1/3}$, where L_{out} is the outer scale of the turbulence. Armstrong et al. (1995, see also Armstrong et al. 1981) estimated that L_{out} is definitely greater than 10^{15} cm, and likely $> 10^{20}$ cm, whereas the largest scale r of interest for observations of Sgr A* is $\sim 10^9$ cm. Thus, eddies on the scales of interest have axis ratios of at least 100:1, which we may safely model as infinitely anisotropic.

Table 1. Regimes of interferometric imaging of scatter broadening (after Narayan & Goodman 1989; Goodman & Narayan 1989).

	Ensemble Average	Average	Snapshot
Integration Time	$t_{\text{int}} \gg t_{\text{ref}}$	$t_{\text{ref}} \gg t_{\text{int}} \gg t_{\text{dif}}$	$t_{\text{dif}} \gg t_{\text{int}}$
Bandwidth	$\frac{\Delta\nu}{\nu} \gg 1$	$1 \gg \frac{\Delta\nu}{\nu} \gg \frac{r_{\text{dif}}^2}{r_{\text{ref}}^2}$	$\frac{r_{\text{dif}}^2}{r_{\text{ref}}^2} \gg \frac{\Delta\nu}{\nu}$
Source Size	...	$\theta_{\text{src}} \lesssim \frac{\lambda}{r_{\text{dif}}} \simeq \theta_{\text{scat}}$	$\theta_{\text{src}} \lesssim \frac{r_{\text{dif}}}{D} \simeq \left(\frac{r_{\text{dif}}}{r_{\text{ref}}}\right) \theta_{\text{scat}}$

Making use of the above assumptions, we write the differential contribution to the power spectrum of fluctuations from a layer at depth z along the line-of-sight as

$$\frac{dQ(\vec{q})}{dz} = Q_z(qr_{\text{in}})^{-(\alpha+2)} \exp(-q^2 r_{\text{in}}^2) \delta(\phi_q - \phi_z). \quad (12)$$

Here, the (two-dimensional) transverse wave-vector \vec{q} has been written in polar form, with q representing the magnitude of \vec{q} and ϕ_q its orientation, Q_z measures the strength of the scattering per unit distance along the line-of-sight, and ϕ_z indicates the direction along which the anisotropic phase fluctuations are oriented. Given the nature of MHD turbulence, ϕ_z is oriented orthogonal to the projected direction of the magnetic field in the layer under consideration.

We assume that all layers in the scattering screen can be described by the same spectral index α and inner scale r_{in} , because all infinitesimal layers are different realizations of the same underlying turbulence. The only two properties that we allow to vary between different layers are the amplitude of fluctuations Q_z and the orientation of the anisotropy ϕ_z . The delta-function in equation (12) indicates that we take the anisotropy within each layer to be infinite.

Substituting equation (12) into equations (2) and (3), and writing \vec{r} in polar coordinates (r, ϕ), we obtain

$$\begin{aligned} \frac{dD_\phi(\vec{r})}{dz} &= \frac{\lambda^2 Q_z}{2\pi^2} \int (qr_{\text{in}})^{-(\alpha+2)} \exp(-q^2 r_{\text{in}}^2) [1 - \cos(\vec{q} \cdot \vec{r})] \\ &\quad \delta(\phi_q - \phi_z) d^2q \\ &= \frac{\lambda^2 Q_z}{2\pi^2 r_{\text{in}}^2} \int_0^\infty q'^{-(\alpha+1)} \exp(-q'^2) \\ &\quad \left[1 - \cos\left(q' \frac{r}{r_{\text{in}}} \cos(\phi - \phi_z)\right) \right] dq' \\ &= \frac{4C}{\alpha} \left[M\left(-\frac{\alpha}{2}, \frac{1}{2}, -\frac{r^2}{4r_{\text{in}}^2} \cos^2(\phi - \phi_z)\right) - 1 \right], \quad (13) \end{aligned}$$

where $q' \equiv qr_{\text{in}}$, M is the Kummer (or confluent hypergeometric) function and we have defined the coefficient C to be

$$C \equiv \frac{\lambda^2 Q_z \Gamma\left(1 - \frac{\alpha}{2}\right)}{8\pi^2 r_{\text{in}}^2}. \quad (14)$$

In order to calculate the phase structure function for the scattering screen, we need to integrate equation (13) over the

line-of-sight depth z of the screen, i.e.,

$$D_\phi(\vec{r}) = \int_0^{z_0} \frac{dD_\phi(\vec{r})}{dz} dz. \quad (15)$$

In writing this integral, we assume that both the strength of perturbations per unit distance, Q_z , and the orientation of anisotropy ϕ_z vary with the line-of-sight coordinate z . In principle, as the magnetic field orientation wanders along the line-of-sight, those two functions may be non-monotonic. However, we can rewrite the integral in a more tractable form by introducing an appropriately averaged amplitude \bar{Q}_z in the definition (14) of C and a normalized probability density $P(\phi_z)$ that measures the relative frequency of layers in the scattering screen that are anisotropic along a particular orientation ϕ_z . With these definitions, we can write the phase structure function as

$$D_\phi(\vec{r}) = \int_0^{2\pi} \frac{dD_\phi(\vec{r})}{dz} P(\phi_z) d\phi_z. \quad (16)$$

Equivalently, we can write the integrated power spectrum of perturbations along the line-of-sight as

$$Q(\vec{q}) = \int_0^{2\pi} \frac{dQ(\vec{q})}{dz} P(\phi_z) d\phi_z. \quad (17)$$

The integral in (16) is difficult to evaluate analytically even for simple forms of the probability distribution function. Analytical results are possible in certain asymptotic limits, which we now discuss. Calculating these limits allows us, in the following section, to write the anisotropic scattering model in terms of quantities that are useful in fitting observational data.

3.1. The quadratic limit $r \ll r_{\text{in}}$

We first consider the limit of small transverse distances, $r \ll r_{\text{in}}$, and use the series expansion

$$M(a, b, z) = 1 + \frac{a}{b} z + \frac{a(a+1)}{b(b+1)} \frac{z^2}{2!} + \dots, \quad (18)$$

to obtain

$$D_\phi(\vec{r}) \simeq C \left[\int_0^{2\pi} \cos^2(\phi - \phi_z) P(\phi_z - \phi_0) d\phi_z \right] \frac{r^2}{r_{\text{in}}^2}. \quad (19)$$

In this last expression, we wrote the probability distribution function in a general form that encapsulates the fact that we will choose below models that are peaked and symmetric around a preferred orientation at an angle ϕ_0 , i.e.,

$$P(\phi_z - \phi_0) = P(\phi_0 - \phi_z). \quad (20)$$

They will also be point symmetric around the origin, i.e.,

$$P(\phi_z - \phi_0) = P(\phi_z - \phi_0 + \pi) \quad (21)$$

in order for the phase structure function (being the Fourier transform of the power spectrum) to be real.

We can use these assumed properties of the probability distribution function to write equation (19) (after making the change of variables $\phi_z = \phi_0 + \phi'$) as

$$\begin{aligned} D_\phi(\vec{r}) &= \mathcal{C} \left[\int_0^{2\pi} \frac{1 + \cos(2\phi - 2\phi_z)}{2} P(\phi_z - \phi_0) d\phi_z \right] \frac{r^2}{r_{\text{in}}^2} \\ &= \frac{\mathcal{C}}{2} \left\{ 1 + \cos(2\phi - 2\phi_0) \int_0^{2\pi} \cos(2\phi') P(\phi') d\phi' \right. \\ &\quad \left. + \sin(2\phi - 2\phi_0) \int_0^{2\pi} \sin(2\phi') P(\phi') d\phi' \right\} \frac{r^2}{r_{\text{in}}^2} \\ &= \frac{\mathcal{C}}{2} \{ 1 + \zeta_0 \cos[2(\phi - \phi_0)] \} \frac{r^2}{r_{\text{in}}^2}, \end{aligned} \quad (22)$$

where

$$\zeta_0 \equiv \int_0^{2\pi} \cos(2\phi_z) P(\phi_z) d\phi_z. \quad (23)$$

As expected, the structure function in this limit increases quadratically with r and has the characteristic angular dependence given in equation (22). In this limit, the form of the phase structure function does not depend on the particular model for the wandering of the magnetic field. The latter only determines the degree of anisotropy via equation (23).

For simplicity in our notation, we will denote the phase structure function along the orientation of anisotropy ϕ_0 (i.e., the major axis) by

$$D_{\text{maj}}(r) \equiv D_\phi(r, \phi = \phi_0) = \frac{\mathcal{C}(1 + \zeta_0)}{2} \frac{r^2}{r_{\text{in}}^2}, \quad (24)$$

and perpendicular to this orientation by

$$D_{\text{min}}(r) \equiv D_\phi(r, \phi = \phi_0 + \pi/2) = \frac{\mathcal{C}(1 - \zeta_0)}{2} \frac{r^2}{r_{\text{in}}^2}. \quad (25)$$

Clearly, in this limit

$$D_{\text{maj}}(r) + D_{\text{min}}(r) = \mathcal{C} \frac{r^2}{r_{\text{in}}^2}. \quad (26)$$

3.2. The limit $r \gg r_{\text{in}}$

In the opposite limit of large transverse distances, $r \gg r_{\text{in}}$, we use the corresponding asymptotic expansion

$$M(a, b, z) \approx \frac{\Gamma(b) \exp(z) z^{(a-b)}}{\Gamma(a)} + \frac{\Gamma(b) (-z)^{-a}}{\Gamma(b-a)}. \quad (27)$$

The second term dominates, so we find

$$D_\phi(\vec{r}) \approx \frac{2^{2-\alpha} \sqrt{\pi} \mathcal{C}}{\alpha \Gamma[(1+\alpha)/2]} \left[\int_0^{2\pi} |\cos(\phi - \phi_z)|^\alpha P(\phi_z - \phi_0) d\phi_z \right] \left(\frac{r}{r_{\text{in}}} \right)^\alpha \quad (28)$$

In this limit, the structure function increases as r^α rather than as r^2 .

The functional form of the above integral depends sensitively on the functional form of the model for the wandering of the magnetic field. However, for reasons that will become apparent below, we will write the phase structure function along the orientation of anisotropy ϕ_0 as

$$\begin{aligned} D_{\text{maj}}(r) &= D_\phi(r, \phi = \phi_0) = \frac{2^{2-\alpha} \sqrt{\pi} \mathcal{C}}{\alpha \Gamma[(1+\alpha)/2]} \\ &\quad \left[\int_0^{2\pi} |\cos(\phi_0 - \phi_z)|^\alpha P(\phi_z - \phi_0) d\phi_z \right] \left(\frac{r}{r_{\text{in}}} \right)^\alpha \\ &= \frac{\mathcal{C}(1 + \zeta_0)}{2} \mathcal{B}_{\text{maj}} \left(\frac{r}{r_{\text{in}}} \right)^\alpha, \end{aligned} \quad (29)$$

where ζ_0 is given by equation (23) and

$$\begin{aligned} \mathcal{B}_{\text{maj}} &\equiv \frac{2^{3-\alpha} \sqrt{\pi}}{\alpha \Gamma[(1+\alpha)/2] (1 + \zeta_0)} \\ &\quad \left[\int_0^{2\pi} |\cos(\phi_0 - \phi_z)|^\alpha P(\phi_z - \phi_0) d\phi_z \right]. \end{aligned} \quad (30)$$

Similarly, we write the phase structure function perpendicular to the orientation of anisotropy as

$$\begin{aligned} D_{\text{min}}(r) &= D_\phi(r, \phi = \phi_0 + \pi/2) = \frac{2^{2-\alpha} \sqrt{\pi} \mathcal{C}}{\alpha \Gamma[(1+\alpha)/2]} \\ &\quad \left[\int_0^{2\pi} |\sin(\phi_0 - \phi_z)|^\alpha P(\phi_z - \phi_0) d\phi_z \right] \left(\frac{r}{r_{\text{in}}} \right)^\alpha \\ &= \frac{\mathcal{C}(1 - \zeta_0)}{2} \mathcal{B}_{\text{min}} \left(\frac{r}{r_{\text{in}}} \right)^\alpha, \end{aligned} \quad (31)$$

where

$$\begin{aligned} \mathcal{B}_{\text{min}} &\equiv \frac{2^{3-\alpha} \sqrt{\pi}}{\alpha \Gamma[(1+\alpha)/2] (1 - \zeta_0)} \\ &\quad \left[\int_0^{2\pi} |\sin(\phi_0 - \phi_z)|^\alpha P(\phi_z - \phi_0) d\phi_z \right]. \end{aligned} \quad (32)$$

3.3. The General Case

In order to facilitate efficient and accurate calculations of the phase structure function in the general case, we devised an approximate analytic expression that bridges the two limiting cases discussed above. We start by writing an approximate expression for the phase structure function along the

major axis of anisotropy as

$$D_{\text{maj}}(r) = \frac{\mathcal{C}(1+\zeta_0)}{2} B_{\text{maj}} \left(\frac{2}{\alpha B_{\text{maj}}} \right)^{-\alpha/(2-\alpha)} \left\{ \left[1 + \left(\frac{2}{\alpha B_{\text{maj}}} \right)^{2/(2-\alpha)} \left(\frac{r}{r_{\text{in}}} \right)^2 \right]^{\alpha/2} - 1 \right\} \quad (33)$$

and perpendicular to it as

$$D_{\text{min}}(r) = \frac{\mathcal{C}(1-\zeta_0)}{2} B_{\text{min}} \left(\frac{2}{\alpha B_{\text{min}}} \right)^{-\alpha/(2-\alpha)} \left\{ \left[1 + \left(\frac{2}{\alpha B_{\text{min}}} \right)^{2/(2-\alpha)} \left(\frac{r}{r_{\text{in}}} \right)^2 \right]^{\alpha/2} - 1 \right\} \quad (34)$$

Using these two approximate expressions, we write the general, approximate form for the phase structure function as

$$D_{\phi}(r, \phi) = \left[\frac{D_{\text{maj}}(r) + D_{\text{min}}(r)}{2} \right] + \left[\frac{D_{\text{maj}}(r) - D_{\text{min}}(r)}{2} \right] \cos[2(\phi - \phi_0)]. \quad (35)$$

Numerical tests show that this fitting function introduces an error no larger than 2% for any value of the ratio r/r_{in} , for values of the power-law index α lying in the physically interesting range between $\alpha = 5/3$ (Kolmogorov) and $\alpha = 2$, and for the various models of the wandering of the magnetic field that we introduce below.

4. PROBABILISTIC MODELS FOR THE WANDERING OF THE DIRECTION OF THE MAGNETIC FIELD

In this section, we describe three different analytic, probabilistic models for the wandering of the direction of the magnetic field along the line of sight in the scattering screen.

4.1. von Mises Model

For most of the calculations below, we use the amphidirectional von Mises distribution (Mardia & Jupp 1999) centered at orientation ϕ_0 and with concentration parameter $k_{\zeta,1}$,

$$P_{\text{vM}}(\phi_z, \phi_0) = \frac{1}{4\pi I_0(k_{\zeta,1})} \left[e^{k_{\zeta,1} \cos(\phi_z - \phi_0)} + e^{k_{\zeta,1} \cos(\phi_z - \phi_0 + \pi)} \right] = \frac{1}{2\pi I_0(k_{\zeta,1})} \cosh[k_{\zeta,1} \cos(\phi_z - \phi_0)], \quad (36)$$

where $I_0(k_{\zeta,1})$ is the modified Bessel function of the first kind and order zero and the denominator is needed to normalize the probability distribution. The von Mises function is a generalization of the Gaussian distribution for circular quantities such as angles, with the concentration parameter $k_{\zeta,1}$ providing a measure of the "peakiness" of the distribution. Note that the power spectrum (17) and the probability distribution (36) need to be point-symmetric around the origin, in order to

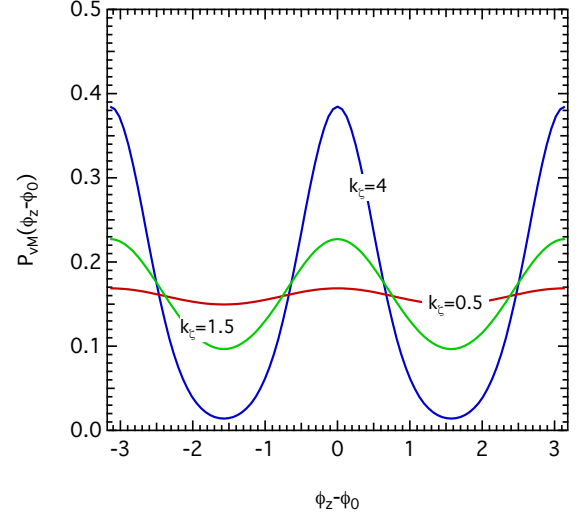


Figure 3. The amphidirectional von Mises distribution for different values of the concentration parameter $k_{\zeta,1}$. The asymmetries of the resulting scattering kernels that correspond to $k_{\zeta} = 0.5, 1.5,$ and 4 are $\mathcal{A} = 1.03, 1.23,$ and $1.91,$ respectively.

describe a real distribution of density inhomogeneities. Figure 3 shows the amphidirectional von Mises distribution for different values of the concentration parameter.

For this model, equation (23) gives

$$\zeta_0 = \frac{I_2(k_{\zeta,1})}{I_0(k_{\zeta,1})}. \quad (37)$$

As we discuss below, for Sgr A*, $\zeta_0 \simeq 3/5$ and plugging this value into the above equation gives $k_{\zeta,1} \simeq 4.38$. Similarly, equation (30) gives

$$B_{\text{maj}} = \frac{2^{3-\alpha} \sqrt{\pi}}{\alpha [I_0(k_{\zeta,1}) + I_2(k_{\zeta,1})]} {}_1\tilde{F}_2 \left(\frac{1+\alpha}{2}; \frac{1}{2}, 1 + \frac{\alpha}{2}; \frac{k_{\zeta,1}^2}{4} \right). \quad (38)$$

where ${}_1\tilde{F}_2$ is the regularized hypergeometric function, and equation (32) gives

$$B_{\text{min}} = \frac{2^{2-\alpha} k_{\zeta,1}}{\alpha I_1(k_{\zeta,1})} {}_0\tilde{F}_1 \left(1 + \frac{\alpha}{2}, \frac{k_{\zeta,1}^2}{4} \right). \quad (39)$$

Both coefficients B_{maj} and B_{min} are equal to unity at $\alpha = 2$ and, for small values of $k_{\zeta,1}$, they scale approximately as α^{-2} down to a value comparable to 2 at $\alpha = 1$. For a Kolmogorov spectrum (i.e., $\alpha = 5/3$) and for the value of the concentration parameter $k_{\zeta,1}$ that we inferred above for Sgr A*, we find $B_{\text{maj}} \simeq 1.54$ and $B_{\text{min}} \simeq 1.79$.

4.2. Dipole model

As a second model, we use the anisotropic scattering model introduced in Johnson & Narayan (2016), which we refer to hereafter as the "dipole" model,

$$P_2(\phi_z - \phi_0; k_{\zeta,2}) = \frac{[1 + k_{\zeta,2} \sin^2(\phi_z - \phi_0)]^{-1-\alpha/2}}{2\pi {}_2F_1(1/2, 1 + \alpha/2, 1, -k_{\zeta,2})}. \quad (40)$$

This expression arises from equation (6) of Johnson & Narayan (2016) that is written in Cartesian coordinates, after making the identification

$$k_{\zeta,2} \equiv \frac{r_{0y}^2}{r_{0x}^2} - 1 \quad (41)$$

and integrating the resulting expression to obtain the normalization constant that appears in the denominator of equation (40).

For this model, equation (23) gives

$$\zeta_0 = \frac{\mathcal{A}^2 - 1}{\mathcal{A}^2 + 1}, \quad (42)$$

where the quantity

$$\mathcal{A}^2 = \frac{{}_2F_1\left(\frac{\alpha+2}{2}, \frac{1}{2}, 2, -k_{\zeta,2}\right)}{{}_2F_1\left(\frac{\alpha+2}{2}, \frac{3}{2}, 2, -k_{\zeta,2}\right)} \quad (43)$$

is related to the asymmetry of the scattering kernel (see §5.1 below). For Sgr A*, $\zeta_0 \simeq 3/5$ and, therefore, $k_{\zeta,2} \simeq 3.52$. Furthermore, equation (30) gives

$$\mathcal{B}_{\text{maj}} = \frac{2^{4-\alpha}}{\alpha^2(1+\zeta_0)\Gamma(\alpha/2)\sqrt{1+k_{\zeta,2}}} \times {}_2F_1\left(\frac{1}{2}, \frac{2+\alpha}{2}, 1, -k_{\zeta,2}\right)^{-1}, \quad (44)$$

and equation (32) gives

$$\mathcal{B}_{\text{min}} = \frac{2^{4-\alpha}}{\alpha^2(1-\zeta_0)\Gamma(\alpha/2)} \times {}_2F_1\left(\frac{1}{2}, -\frac{\alpha}{2}, 1, -k_{\zeta,2}\right)^{-1}, \quad (45)$$

For a Kolmogorov spectrum (i.e., $\alpha = 5/3$) and for the value of the concentration parameter $k_{\zeta,2}$ that we inferred above for Sgr A*, we find $\mathcal{B}_{\text{maj}} \simeq 1.54$ and $\mathcal{B}_{\text{min}} \simeq 1.75$.

4.3. Periodic Boxcar Model

Finally, we also consider a periodic boxcar model of the form

$$P_3(\phi_z - \phi_0; k_{\zeta,3}) = \frac{1+k_{\zeta,3}}{2\pi} \times \begin{cases} 1, & \text{if } (1+k_{\zeta,3})|\phi_z - \phi_0 + n\pi| \leq \pi/2; \quad n = \dots, -1, 0, 1, \dots \\ 0, & \text{otherwise} \end{cases} \quad (46)$$

with the concentration parameter $k_{\zeta,3}$ defined in a way analogous to the earlier two models, i.e., $k_{\zeta,3} = 0$ corresponds to an isotropic angular model and the degree of anisotropy increases with $k_{\zeta,3}$.

For this model, equation (23) gives

$$\zeta_0 = \frac{1+k_{\zeta,3}}{\pi} \sin\left(\frac{\pi k_{\zeta,3}}{1+k_{\zeta,3}}\right) \quad (47)$$

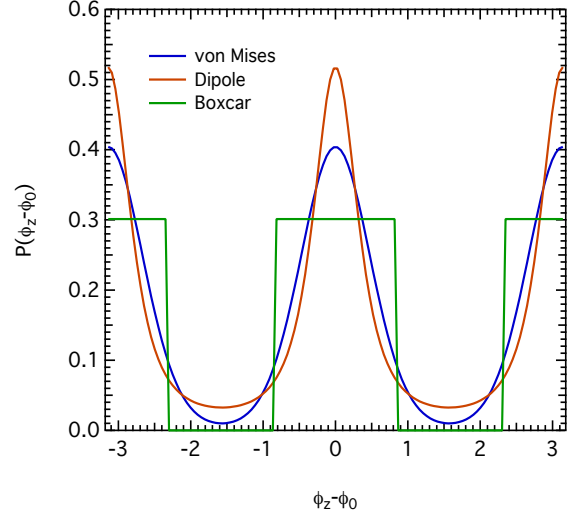


Figure 4. The three models for the angular distribution of the power spectrum of fluctuations in the scattering screen towards Sgr A*. Model 1 is an amphidirectional von Mises distribution, Model 2 is the dipole model of Johnson & Narayan (2016), and Model 3 is a periodic boxcar distribution. For each model, the concentration parameter is chosen such that the anisotropy of the scattering kernel at long wavelengths matches that of Sgr A*.

For Sgr A*, $\zeta_0 = 3/5$ and, therefore, $k_{\zeta,3} \simeq 0.89$. Equations (30) and (32) can be also be integrated analytically in terms of hypergeometric functions. However, the expressions are long and unwieldy. As a result, these expressions are best evaluated numerically. For a Kolmogorov spectrum (i.e., $\alpha = 5/3$) and for the value of the concentration parameter $k_{\zeta,3}$ that we inferred above for Sgr A*, we find $\mathcal{B}_{\text{maj}} \simeq 1.55$ and $\mathcal{B}_{\text{min}} \simeq 1.85$.

Figure 4 compares the detailed functional form of the three different angular models for values of the concentration parameters that give rise to a two-to-one anisotropy in the scattering kernel at very long wavelengths (see below).

4.4. Approximate Expressions

Using a combination of Taylor expansions and Padé approximations, we found a number of approximate relations for the anisotropy parameter ζ_0 and the two coefficients \mathcal{B}_{maj} and \mathcal{B}_{min} , with an accuracy $\lesssim 1\%$ for $k_{\zeta} \leq 10$ and $3/2 \leq \alpha \leq 2$.

We write the anisotropy parameter ζ_0 , for all models, as

$$\zeta_0 = \frac{\sum_{i=0}^6 \zeta_{u,i} k_{\zeta}^i}{\sum_{i=0}^6 \zeta_{d,i} k_{\zeta}^i}. \quad (48)$$

We write the coefficient \mathcal{B}_{maj} , for all models, as

$$\mathcal{B}_{\text{maj}} = \frac{2^{3-\alpha}}{\alpha\Gamma(1+\alpha/2)} \left[2\alpha - 3 - 2(\alpha-2) \frac{\sum_{i=0}^6 \mathcal{B}_{u,i} k_{\zeta}^i}{\sum_{i=0}^6 \mathcal{B}_{d,i} k_{\zeta}^i} \right], \quad (49)$$

Finally, we write a similar expression for the coefficient \mathcal{B}_{\min} for the dipole model, i.e.,

$$\mathcal{B}_{\min} = \frac{2^{3-\alpha}}{\alpha\Gamma(1+\alpha/2)} \left[2\alpha - 3 - 2(\alpha-2) \frac{\sum_{i=0}^6 \mathcal{M}_{u,i} k \zeta^i}{\sum_{i=0}^6 \mathcal{M}_{d,i} k \zeta^i} \right], \quad (50)$$

but, for the von Mises and boxcar models, we write

$$\mathcal{B}_{\min} = \frac{2^{3-\alpha}}{\alpha\Gamma(1+\alpha/2)} \left[\frac{\sum_{i=0}^6 \mathcal{M}_{u,i} k \zeta^i}{\sum_{i=0}^6 \mathcal{M}_{d,i} k \zeta^i} \right]^{-2(\alpha-2)}, \quad (51)$$

The coefficients of the Padé approximations for the various expressions and for the three models are given in the Appendix.

5. ENSEMBLE-AVERAGE VISIBILITIES

With the definitions discussed in the previous two sections, we can now calculate the effects of interstellar scattering on the images of scatter-broadened sources and the corresponding interferometric observables. In this and in the following sections, we will mostly use the framework and notation of Johnson & Narayan (2016).

If we denote by \vec{b} the baseline between two stations of an interferometric array, by $V_{\text{ea}}(\vec{b})$ the complex ensemble-average visibility measured on this baseline, and by $V_{\text{src}}(\vec{b})$ the complex visibility of the unscattered source, then (Coles et al. 1987)

$$V_{\text{ea}}(\vec{b}) = V_{\text{src}}(\vec{b}) \exp \left[-\frac{1}{2} D_\phi \left(\frac{\vec{b}}{1+M} \right) \right]. \quad (52)$$

Hereafter, we will use $b = |\vec{b}|$ to denote the length of the baseline vector. We will consider first the two limiting cases, $b \ll r_{\text{in}}$ and $b \gg r_{\text{in}}$.

5.1. The $b \ll r_{\text{in}}$ regime

At long wavelengths (i.e., greater than a few cm in the case of Sgr A*), where we expect $b \ll r_{\text{in}}$, the ensemble average visibility reduces to (see eq. [22])

$$\lim_{r_{\text{diff}} \ll r_{\text{in}}} V_{\text{ea}}(\vec{b}) = V_{\text{src}}(\vec{b}) \exp \left[-\frac{\mathcal{C}}{4(1+M)^2} \left(\frac{b}{r_{\text{in}}} \right)^2 \times \{1 + \zeta_0 \cos[2(\phi - \phi_0)]\} \right]. \quad (53)$$

Traditionally, the ensemble-average visibility amplitude of a scatter-broadened source is modeled in terms of an anisotropic function of the form (Narayan & Goodman 1989; Bower et al. 2004)

$$V_{\text{ea}}(u', v') = V_{\text{src}}(u', v') \exp \left\{ -\frac{\pi^2}{4 \ln 2} \left[(u' \theta_{\text{maj}})^{\beta-2} + (v' \theta_{\text{min}})^{\beta-2} \right] \right\}, \quad (54)$$

where u' and v' are baseline lengths in units of the wavelength of observations in a coordinate system rotated to

match the position angle ϕ_{PA} of the scattered image, and θ_{maj} and θ_{min} are the FWHM angular sizes of the scattered image along the major and the minor axis of anisotropy, respectively. For anisotropic scattering, we also define the degree of anisotropy of the scattering kernel as the ratio of the angular sizes along the major and minor axis of the kernel, i.e.,

$$A \equiv \frac{\theta_{\text{maj}}}{\theta_{\text{min}}}. \quad (55)$$

The case considered in this subsection, $b \ll r_{\text{in}}$, corresponds to $\beta = 4$ (structure function varying quadratically with distance). Rotating the coordinate system to the usual (u, v) plane, with the position angle ϕ_0 measured as an angle North of East, and transforming to polar coordinates, $(u, v) \equiv (b/\lambda)(\cos \phi, \sin \phi)$, we can write expression (54) as

$$V_{\text{ea}}(\vec{b}) = V_{\text{src}}(\vec{b}) \exp \left[-\frac{\pi^2 b^2 \theta_{\text{maj}}^2}{\lambda^2 (8 \ln 2)} \left(\frac{A^2 + 1}{A^2} \right) \left(1 + \frac{A^2 - 1}{A^2 + 1} \cos[2(\phi - \phi_0)] \right) \right]. \quad (56)$$

In order to put this expression in the same form as equation (53), we identify

$$\lim_{b \ll r_{\text{in}}} A = \left(\frac{1 + \zeta_0}{1 - \zeta_0} \right)^{1/2}, \quad (57)$$

so that

$$V_{\text{ea}}(\vec{b}) = V_{\text{src}}(\vec{b}) \exp \left[-\frac{\pi^2 b^2 \theta_{\text{maj}}^2}{\lambda^2 (4 \ln 2)} \left(\frac{1 + \zeta_0 \cos[2(\phi - \phi_0)]}{1 + \zeta_0} \right) \right]. \quad (58)$$

Comparing equations (53) and (58), we find that the angular size of a scatter-broadened point source along the major axis of anisotropy, at some wavelength λ_0 that satisfies the limit $b \ll r_{\text{in}}$, is

$$\begin{aligned} \theta_{\text{maj},0} &= \sqrt{4 \ln 2 (1 + \zeta_0) \mathcal{C}} \frac{\lambda_0}{(1+M)r_{\text{in}}} \\ &= \left[\frac{(1 + \zeta_0) \bar{Q}_z \Gamma(1 - \alpha/2) \ln 2}{2} \right]^{1/2} \frac{\lambda_0^2}{(1+M)\pi r_{\text{in}}^2}, \end{aligned} \quad (59)$$

where, in the last expression, we used relation (14). We can solve equation (59), using also the definitions (55) and (57), to express the amplitude of the power spectrum of turbulence in terms of the angular sizes of the scattering kernel at some reference wavelength λ_0 as

$$\bar{Q}_z = \frac{(1+M)^2 \pi^2 (\theta_{\text{maj},0}^2 + \theta_{\text{min},0}^2)}{\Gamma(1 - \alpha/2) \ln 2} \left(\frac{r_{\text{in}}}{\lambda_0} \right)^4. \quad (60)$$

For the scattering screen towards Sgr A*, in this limit, $A \simeq 2$ (see, e.g., Bower et al. 2004, 2006). Therefore, $\zeta_{\text{SGRA},0} \simeq 3/5$. Furthermore, connecting equation (59) to equation (6) and setting $M = (2.7 \text{ kpc})/(5.6 \text{ kpc}) \simeq 0.5$, as inferred from

observations of the Galactic Center magnetar (Bower et al. 2014a), we obtain

$$\bar{Q}_z = 2.5 \times 10^{-12} \left[\Gamma \left(1 - \frac{\alpha}{2} \right) \right]^{-1} \left(\frac{r_{\text{in}}}{\text{cm}} \right)^4. \quad (61)$$

Note that, in principle, long wavelength observations of the ensemble average visibilities allow us only to infer the ratio $\bar{Q}_z/r_{\text{in}}^4$. Extrapolating the model to smaller wavelengths for which the diffractive scale is comparable to or smaller than the inner scale of turbulence requires an independent measurement of the size of the inner scale.

5.2. The $b \gg r_{\text{in}}$ regime

In this regime, the ensemble average visibility cannot be put in the form (54), even if we set $\beta = \alpha + 2$, which is the fitting formula often used. Nevertheless, we can use the general form of the phase structure function, i.e., equation (28), to reach two important conclusions.

First, the orientation of the major axis of the scattering kernel (defined by the angle ϕ_0) does not depend on wavelength. In other words, the position angle for the scattering kernel of Sgr A* measured at long wavelengths can be used even when extrapolating the properties of the scattering screen to the mm-wavelengths of the EHT.

Second, the degree of anisotropy of the scattering kernel evolves with wavelength. It proved impossible to convert the general expression of the phase structure function in this case into a corresponding image and calculate its FWHM along the two axes of the scattering kernel. Instead, in order to get an understanding of the dependence of the characteristic size and anisotropy of the scatter-broadened image on wavelength, we first use equation (52) with the phase structure function along the major and minor axes of the scatter broadened image (eqs. [29] and [31]) to find the baseline lengths b_{maj} and b_{min} for which the exponent in the right-hand side of equation (52) becomes equal to $-(1/2)$, i.e.,

$$b_{\text{maj}} = (1+M)r_{\text{in}} \left[\frac{2}{(1+\zeta_0)\mathcal{B}_{\text{maj}}\mathcal{C}} \right]^{1/\alpha} \quad (62)$$

and

$$b_{\text{min}} = (1+M)r_{\text{in}} \left[\frac{2}{(1-\zeta_0)\mathcal{B}_{\text{min}}\mathcal{C}} \right]^{1/\alpha} \quad (63)$$

These, of course, correspond to the baseline lengths that resolve the diffractive scale of the scattering screen along the major and minor axes of the scatter broadened image. We then use these lengths to define characteristic image sizes via

$$\theta_{\text{maj}} \equiv \sqrt{8 \ln 2} \frac{\lambda}{b_{\text{maj}}} = \sqrt{8 \ln 2} \frac{\lambda}{(1+M)r_{\text{in}}} \left[\frac{(1+\zeta_0)\mathcal{B}_{\text{maj}}\mathcal{C}}{2} \right]^{1/\alpha} \quad (64)$$

and

$$\theta_{\text{min}} \equiv \sqrt{8 \ln 2} \frac{\lambda}{b_{\text{min}}} = \sqrt{8 \ln 2} \frac{\lambda}{(1+M)r_{\text{in}}} \left[\frac{(1-\zeta_0)\mathcal{B}_{\text{min}}\mathcal{C}}{2} \right]^{1/\alpha} \quad (65)$$

Combining these two equations, we can calculate the degree of anisotropy in the limit $b \gg r_{\text{in}}$

$$\lim_{b \gg r_{\text{in}}} A = \left[\frac{(1+\zeta_0)\mathcal{B}_{\text{maj}}}{(1-\zeta_0)\mathcal{B}_{\text{min}}} \right]^{1/\alpha}. \quad (66)$$

This is different than the $b \ll r_{\text{in}}$ regime both because of the exponent being $1/\alpha$ as opposed to $1/2$ and because, in general, $\mathcal{B}_{\text{maj}}/\mathcal{B}_{\text{min}} \neq 1$.

5.3. The General Case

In the general case, we write the ensemble average visibility (52) using the approximate expression (35) for the phase structure function. We then follow the same procedure as in equations (62) and (63) to find the baseline lengths that resolve the diffractive scale along the major and minor axes of anisotropy as

$$b_{\text{maj}} = (1+M)r_{\text{in}} \left(\frac{2}{\alpha\mathcal{B}_{\text{maj}}} \right)^{1/(\alpha-2)} \left\{ \left[1 + 4^{1/(2-\alpha)} \frac{\mathcal{B}_{\text{maj}}^{2/(\alpha-2)} \alpha^{\alpha/(\alpha-2)}}{\mathcal{C}(1+\zeta_0)} \right]^{2/\alpha} - 1 \right\}^{1/2} \quad (67)$$

and

$$b_{\text{min}} = (1+M)r_{\text{in}} \left(\frac{2}{\alpha\mathcal{B}_{\text{min}}} \right)^{1/(\alpha-2)} \left\{ \left[1 + 4^{1/(2-\alpha)} \frac{\mathcal{B}_{\text{min}}^{2/(\alpha-2)} \alpha^{\alpha/(\alpha-2)}}{\mathcal{C}(1-\zeta_0)} \right]^{2/\alpha} - 1 \right\}^{1/2} \quad (68)$$

the corresponding image sizes as

$$\theta_{\text{maj}} \equiv \sqrt{8 \ln 2} \frac{\lambda}{b_{\text{maj}}} \quad (69)$$

and

$$\theta_{\text{min}} \equiv \sqrt{8 \ln 2} \frac{\lambda}{b_{\text{min}}} \quad (70)$$

and the degree of anisotropy using equation (55).

Figure 5 shows the wavelength dependence of the major axis of the scattering kernel for Sgr A* as well as its anisotropy for a Kolmogorov spectrum of fluctuations ($\alpha = 5/3$), for the three models of magnetic-field wandering, and for the parameters we obtained in §4.1. Depending on the (unknown) inner scale of turbulence in the scattering screen, the size of the scattering kernel at the EHT wavelengths may be reduced by as much as 50% from the simple extrapolation of the λ^2 dependence found at long wavelengths. Also, the degree of anisotropy of the scattering kernel increases with decreasing wavelength, depending again on the inner scale of turbulence. Even though the major axis of the scattering kernel depends very weakly on the angular model, the minor

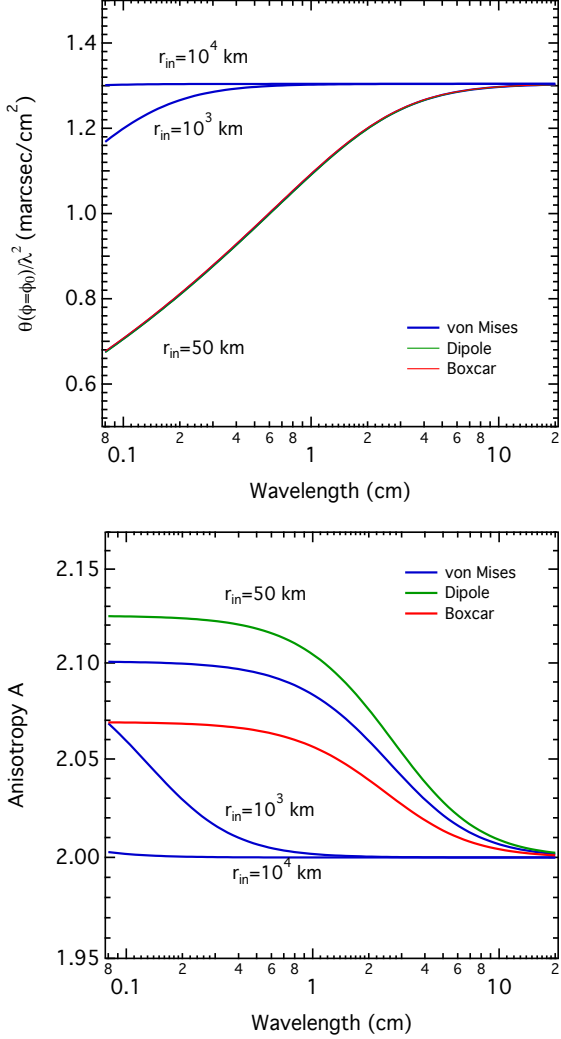


Figure 5. (Top) The characteristic size of the scattering kernel for Sgr A*, along its major axis, divided by the square of the wavelength, as a function of wavelength. (Bottom) The degree of anisotropy of the scattering kernel, defined as the ratio of its major to minor axis. The power spectrum of fluctuations is assumed to be Kolmogorov ($\alpha = 5/3$), with the remaining parameters of the screen inferred from long-wavelength observations (see §5.1). The blue curves correspond to three different choices for the inner scale of turbulence r_{in} in the scattering screen. Depending on r_{in} , the scattering kernel at short wavelengths becomes smaller and more anisotropic compared to what a simple extrapolation from long wavelengths predicts. The different colors correspond to the three models for the wandering of the direction of anisotropy for $r_{\text{in}} = 50$ km. Even though the major axis of the scattering kernel depends very weakly on the angular model, the minor axis and, hence, the anisotropy, does depend at the $\sim 5\%$ level.

axis and, hence, the anisotropy, does depend weakly on them at the $\sim 5\%$ level.

Figure 6 shows the dependence of the scattering kernel on baseline length at a wavelength of 1.3 mm; all other parameters are the same as in Figure 5. As expected from the above discussion, the size of the scattering kernel, which determines the baseline at which the visibility cuts off, varies with the choice of r_{in} . Moreover, the functional form of the scattering kernel evolves with wavelength, becoming shallower (in $u-v$ space) once the diffractive length becomes larger than the inner scale of turbulence. The largest EHT baselines are $\simeq 6G\lambda$ and $\simeq 9G\lambda$ in the E-W and N-S directions, respectively. As a result, the effects of a finite inner scale of turbulence may significantly affect the interpretation and deblurring of EHT observations of Sgr A*.

6. REFRACTIVE EFFECTS

In the average image regime, which is relevant for single-epoch VLBI observations of Sgr A*, the images and interferometric observables will exhibit fluctuations due to refractive effects (Narayan & Goodman 1989; Goodman & Narayan 1989; Gwinn et al. 2014; Johnson & Gwinn 2015; Johnson & Narayan 2016). These effects are dominated by density fluctuations on scales comparable to the refractive scale $\simeq r_{\text{ref}}$. Because of the large separation between the diffractive and refractive scales (see Fig. 2), one can estimate the refractive effects using a simplified formalism for scattering developed originally for pulsars by Blandford & Narayan (1985) and applied recently to extended sources and interferometry by Johnson & Narayan (2016).

In this framework, the variance of the complex visibility on baseline \vec{b} caused by refractive substructure is estimated by the following expression (see eq. 16 of Johnson & Narayan 2016),

$$\sigma_{\text{ref}}^2 \approx \frac{\lambda^2 r_{\text{F}}^4}{4\pi^2} \int d^2\vec{q} \left[\vec{q} \cdot \left(\vec{q} + \frac{\vec{b}}{D\lambda} \right) \right]^2 \left| V_{\text{ea}} \left(D\lambda\vec{q} + \vec{b} \right) \right|^2 Q(\vec{q}). \quad (71)$$

For comparison with VLBI observations, this expression must be modified to remove the variance that arises from modulation of the total image flux density and image wander (caused, respectively, by refractive focusing/defocusing and an overall ray deflection; Blandford & Narayan 1985). These effects are degenerate with standard VLBI calibration (in the absence of absolute flux calibration and absolute phase referencing, which are challenging at high frequencies). Thus, we will also define the *renormalized refractive noise*, which removes these two contributions. For example, the renormalized refractive noise on a zero baseline is zero because all variations on this baseline reflect modulation of the total flux density. Differences between the total refractive noise and the renormalized refractive noise are significant for baselines that do not heavily resolve the source.

Because of the complexity of the integrals in equation (71), we evaluate them numerically, using the approximate expression (35) for the ensemble averaged visibility, but the complete expressions for the power spectra. The refractive variance on a given baseline depends on three parameters: the

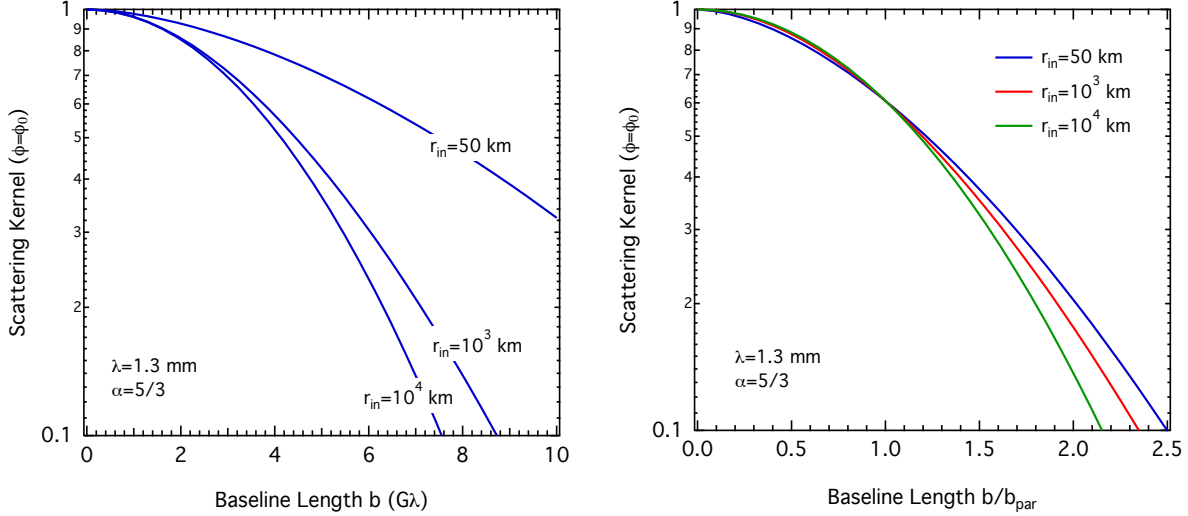


Figure 6. The scattering kernel of Sgr A*, along its major axis, at 1.3 mm. All other parameters are the same as in Figure 5. In the left panel, the kernel is plotted as a function of baseline length in units of $G\lambda$; in the right panel, the baseline lengths have been normalized to the characteristic length b_{maj} given by equation (67). A smaller inner scale of turbulence leads to reduced broadening, and also alters the functional form of the scattering kernel.

power-law index of turbulence α , the ratio of the characteristic baseline length b_{maj} (see eq.[67]) that resolves the image along the direction of anisotropy ($\phi = \phi_0$) to the inner scale of turbulence,

$$\mu_d \equiv \frac{b_{\text{maj}}}{r_{\text{in}}}, \quad (72)$$

and the ratio

$$\rho_0 \equiv \frac{D\lambda}{r_{\text{in}}^2} = (1+M) \left(\frac{r_{\text{F}}}{r_{\text{in}}} \right)^2, \quad (73)$$

which measures the number of circular patches of size equal to r_{in} that fits within a Fresnel circle. For Sgr A*, at $\lambda = 1$ cm,

$$\rho_0 \simeq 1.3 \times 10^5 (1+M) \left(\frac{D}{2.7 \text{ kpc}} \right) \left(\frac{\lambda}{1 \text{ cm}} \right) \left(\frac{r_{\text{in}}}{10^3 \text{ km}} \right)^{-2}. \quad (74)$$

Figure 7 shows the dependence of the rms refractive visibility on baseline length for a point source, and for parameters that are expected for Sgr A*. At small baseline lengths, the major cause of rms visibility fluctuations is flux variations and image wandering, neither of which is observable by a mm-VLBI experiment such as the EHT. On the other hand, at baseline lengths larger than the diffractive scale, the rms visibility is primarily caused by the refractive substructure in the image introduced by scattering and attains a characteristic power-law dependence on baseline length. In general, the rms refractive visibility at large baselines is higher along the major axis of anisotropy, since there is more power of density fluctuations along that orientation.

In Figure 7, the baseline length is normalized to the characteristic baseline length b_{maj} (see eq.[67]) that resolves the image along the direction of anisotropy ($\phi = \phi_0$). For this

reason, the transition to the power-law dependence occurs at longer baseline lengths for orientations that are perpendicular to the direction of anisotropy ($\phi = \phi_0 + \pi/2$), since the corresponding diffractive scale is larger.

Figure 8 shows the dependence of the rms refractive visibility for a long baseline ($b = 12b_{\text{maj}}$) on the ratio μ_d of the characteristic baseline length b_{maj} to the inner scale of turbulence. It also compares the numerical results to the analytical expressions derived by Goodman & Narayan (1989) for the case of isotropic scattering in two regimes, depending on whether the diffractive scale is larger or smaller than the inner scale of turbulence ($\mu_d \ll 1$ or $\mu_d \gg 1$). In our notation, these two expressions become for $\mu_d \ll 1$,

$$\sigma_{\text{ref}} = \left[2^{\alpha-2} \frac{\Gamma(1+\alpha/2)}{\Gamma(1-\alpha/2)} \right]^{1/2} \left(\frac{\rho_0}{1+M} \right)^{\alpha/2-1} \mu^{-\alpha/2} \mu_d^{1-\alpha/2}, \quad (75)$$

and for $\mu_d \gg 1$,

$$\sigma_{\text{ref}} = \left[2^{\alpha-2} \frac{\Gamma(1+\alpha/2)\Gamma(4/\alpha)}{\Gamma(1-\alpha/2)} \right]^{1/2} \left(\frac{\rho_0}{1+M} \right)^{\alpha/2-1} \mu^{-\alpha/2} \mu_d^{2-\alpha}, \quad (76)$$

where $\mu \equiv b/b_{\text{maj}}$. As Figure 8 shows, the dependence of the rms refractive visibility on the ratio $\mu_d = b_{\text{maj}}/r_{\text{in}}$ follows, in all orientations, the general trend exhibited in the case of isotropic scattering. However, as expected, the rms refractive visibility is, in general, larger parallel to the major scattering axis and smaller perpendicular to it than what the above expressions predict. This is a direct consequence of the angular dependence of the power spectrum of density fluctuations, which determines both the anisotropy in the scattering kernel and the amplitude of refractive fluctuations.

We now turn to an important feature of refractive effects. To recall, equation (35) shows that the scattering kernel that

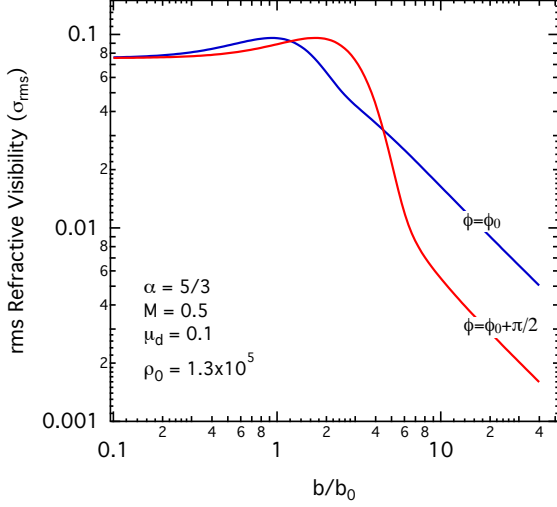


Figure 7. The rms refractive visibility (σ_{ref}) as a function of baseline length for parameters of the scattering screen that are typical for Sgr A* at mm-wavelengths. The blue and red curves show the result for orientations that are parallel and perpendicular to axis of anisotropy. In both cases, the baseline length is normalized to the characteristic baseline length b_{maj} (see eq.[67]) that resolves the image along the direction of anisotropy (i.e., at $\phi = \phi_0$). At large baselines, the rms refractive visibility is higher along the direction of anisotropy, which corresponds (by definition) to a larger amplitude of density fluctuations in the scattering screen.

figures in the ensemble average visibilities depends primarily on the overall image anisotropy parameter A ; it is insensitive to the detailed angular dependence of the power spectrum of density fluctuations, $P(\phi_z, \phi_0)$. By contrast, the rms fluctuations in refractive visibilities depend very strongly on $P(\phi_z, \phi_0)$. Figure 9 shows the angular dependence of the rms refractive visibility for parameters typical of the scattering screen towards Sgr A*, for the three different models of the angular power spectrum. Clearly, the model of the power spectrum with the box-car angular distribution results in zero refractive visibilities at angles perpendicular to the major axis of the scattering kernel. We show, in Figure 11, that the refractive noise does not actually fall to zero because of higher-order terms in the scattering approximation, although the noise is still markedly reduced relative to the von Mises and dipole models (see Figure 13).

We also explored the effects of varying the scattering model by simulating images of the scattering on Gaussian sources. To perform these simulations, we used the `stochastic optics` module of the `eht-imaging`¹ software library, as is described in Johnson (2016).

Figure 11 shows simulated images of a Gaussian source with $\text{FWHM} = 8GM/c^2 \approx 40 \mu\text{as}$ (i.e., the size of Sgr A*

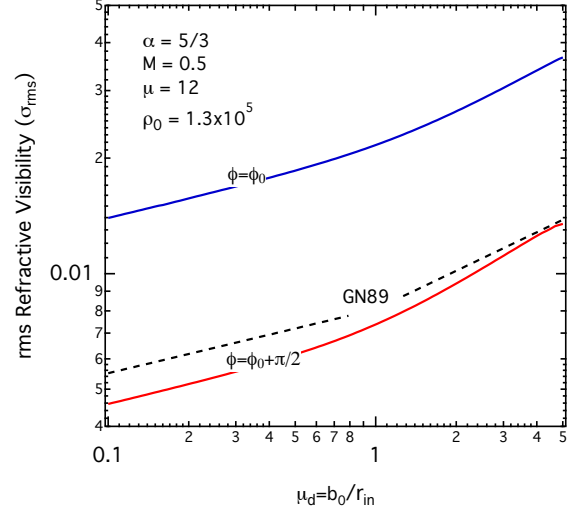


Figure 8. The rms refractive visibility (σ_{ref}) evaluated at $b = 12b_{\text{maj}}$ as a function of the ratio of the characteristic baseline length b_{maj} to the inner scale of turbulence. The parameters of the scattering screen are the same as in Fig 7. The blue and red curves show the result for orientationw that are parallel and perpendicular to the axis of anisotropy. The dotted lines show the expressions derived by Goodman & Narayan (1989) for anisotropic scattering, in the two different regimes $\mu_d \ll 1$ and $\mu_d \gg 1$.

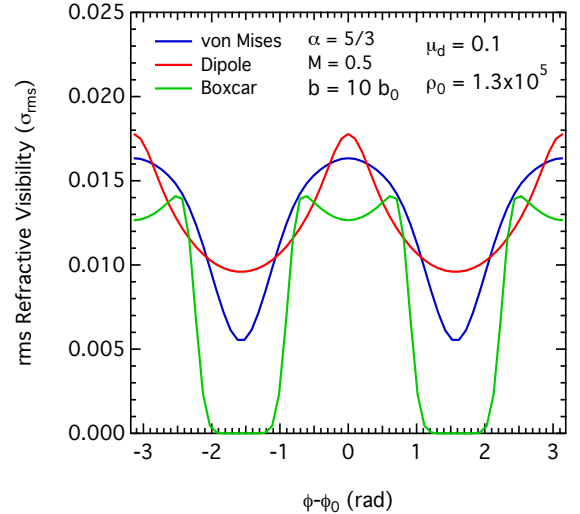


Figure 9. The rms refractive visibility (σ_{ref}) evaluated at $b = 10b_{\text{maj}}$ as a function of the orientation angle with respect to the major axis of the scattering kernel, for the three different models of the angular dependence of the power spectrum of density fluctuations. The parameters of the scattering screen are the same as in Fig 7. The rms of the refractive visibility depends very strongly on the details of the angular dependence of the power spectrum of fluctuations.

¹ <https://github.com/achael/eht-imaging> (Chael et al. 2016).

from EHT observations Doeleman et al. 2008). The scattering parameters were chosen to give scattering that matches

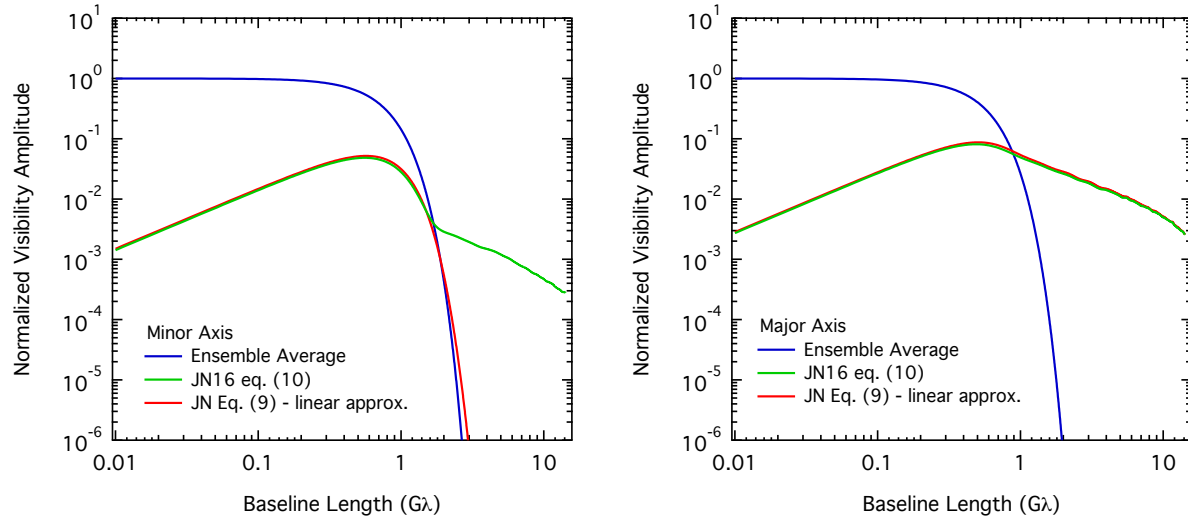


Figure 10. Ensemble-average visibilities and the renormalized refractive noise for Sgr A* at 3 mm with the boxcar model for the magnetic field wandering. Left/right panel shows dependence on baseline length for baselines oriented along the minor/major axis. The plotted curves were calculated from numerical simulations of the scattering (as in later Figures); the refractive noise was estimated using 1000 independent realizations of the scattering. Using the linear approximation (Eq. 10 of Johnson & Narayan 2016) for the scattering simulations results in almost no power for long baselines along the minor axis, as predicted by Eq. 71 (which also uses the linear approximation). However, including the full expression for refractive steering in the simulations (Eq. 9 of Johnson & Narayan 2016) produces a small amount of additional refractive noise along this axis, demonstrating the breakdown of the linear approximation.

observations of Sgr A* at centimeter wavelengths (Bower et al. 2006). The panels show three choices of r_{in} and three models of the angular power distribution. At 1.3 mm, the introduced anisotropy in the scattered images is hardly noticeable because the source size is significantly larger than the scattering kernel. However, the refractive substructure in the image is quite pronounced and becomes stronger with increasing r_{in} . Refractive fluctuations appear qualitatively different for the boxcar model, relative to the other two models.

Figure 11 illustrates the two primary effects of scattering on the image: an overall broadening of the image (“blurring”) by the ensemble-average scattering kernel, and the addition of substructure and distortions on the broadened image. Although image blurring by the ensemble-average scattering kernel could be eliminated using deconvolution schemes such as those described in Fish et al. (2014), refractive substructure will still remain. Eliminating this will require a more sophisticated scheme such as the stochastic optics method described in Johnson (2016).

Figure 12 shows the wavelength dependence of scattering effects, again for three choices of r_{in} , keeping the intrinsic source size the same. Scattering dominates at $\lambda = 3$ mm, to the extent that the anisotropy in the scattering is now quite evident. Refractive effects are also very strong. At $\lambda = 1.3$ mm, the case considered in Figure 11, scattering is less dominant, but refractive substructure is still visible. Finally, at $\lambda = 0.8$ mm, scattering is no longer an issue, except perhaps for the largest inner scale we have considered, $r_{in} = 10^4$ km.

We also used scattering simulations to evaluate the renormalized refractive noise for several cases of interest. Specifi-

cally, we considered observations of Sgr A* at 230 GHz, 85 GHz, and 43 GHz. These frequencies represent standard observing frequencies for the EHT, the Global Millimeter VLBI Array (GMVA), and the Very Long Baseline Array (VLBA). At each frequency, we scattered a circular Gaussian source with size given by the approximate inferred size of Sgr A* at that frequency: $40 \mu\text{as}$ at 230 GHz (e.g., Doeleman et al. 2008), $130 \mu\text{as}$ at 85 GHz (e.g., Ortiz-León et al. 2016), and $300 \mu\text{as}$ at 43 GHz (e.g., Bower et al. 2014b). For each frequency and scattering model, we generated 1000 different scattering screens and produced a scattered image for each. We then normalized and centered each image before computing interferometric visibilities. The spread among the complex visibilities on each baseline then gives the renormalized refractive noise.

Figure 13 shows the renormalized refractive noise for three scattering models for each of these cases with baseline tracks of the corresponding VLBI arrays overplotted. In this figure, the refractive noise is expressed as the root-mean-square fluctuations divided by the zero-baseline flux density. As in Figure 11, the dipole and amphidirectional von Mises models give comparable results, while the boxcar model gives slightly higher refractive noise. For most baselines, the refractive noise is a few percent of the total image flux density, or roughly ~ 100 mJy. If a baseline measures a flux density significantly higher than this value, then the signal must reflect intrinsic source structure.

Figure 14 shows the renormalized refractive noise expressed as a fraction of the ensemble-average flux density on the same baseline. These panels thus show the relative

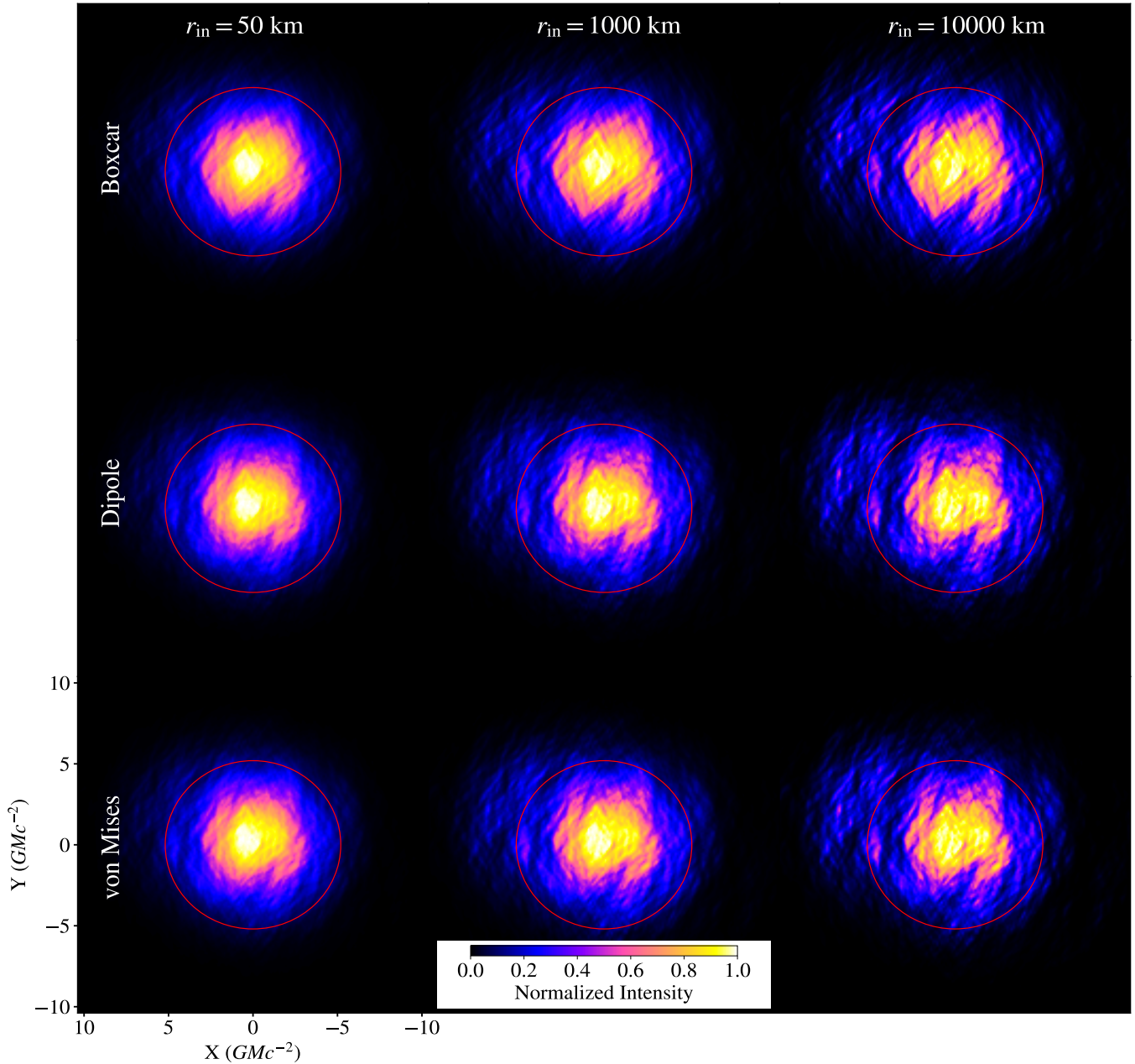


Figure 11. Simulated scattered images of Sgr A* at 1.3 mm. Each image shows a single instantaneous image (i.e., a representative image in the “Average” regime). Columns show representative values of the inner scale (50 km, 1,000 km, and 10,000 km); rows show our three example scattering models. In all cases, the unscattered image is a circular Gaussian with FWHM of $\sim 40 \mu\text{as}$; for reference, the red circle has a diameter of $\sim 50 \mu\text{as}$, comparable to the expected shadow size for Sgr A*. Because the angular broadening is significantly smaller than the angular size of the source, the images are not significantly anisotropic, although refractive substructure is apparent in all cases and is strongest for the boxcar model.

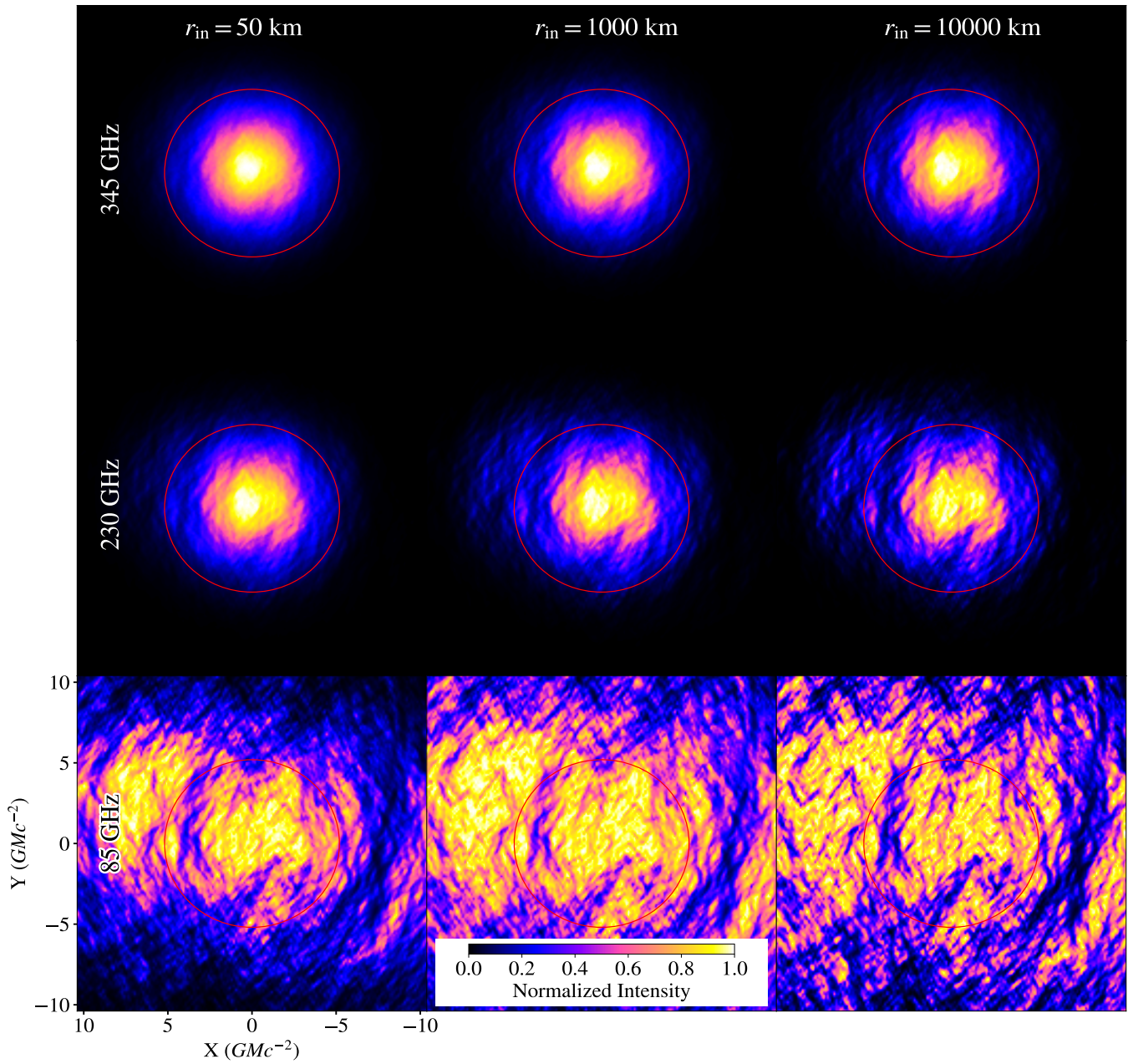


Figure 12. Similar to Figure 11 but with rows showing scattering at 85 GHz (~ 3 mm), 230 GHz (~ 1.3 mm), and 345 GHz (~ 0.8 mm) (here we use the von Mises scattering model in all cases). We again use a $\sim 40 \mu\text{as}$ Gaussian as the unscattered source for each case, and the effects of scattering-induced anisotropy are evident at $\lambda = 3$ mm. Notably, both image blurring and refractive substructure are insignificant at $\lambda = 3$ mm, regardless of the inner scale.

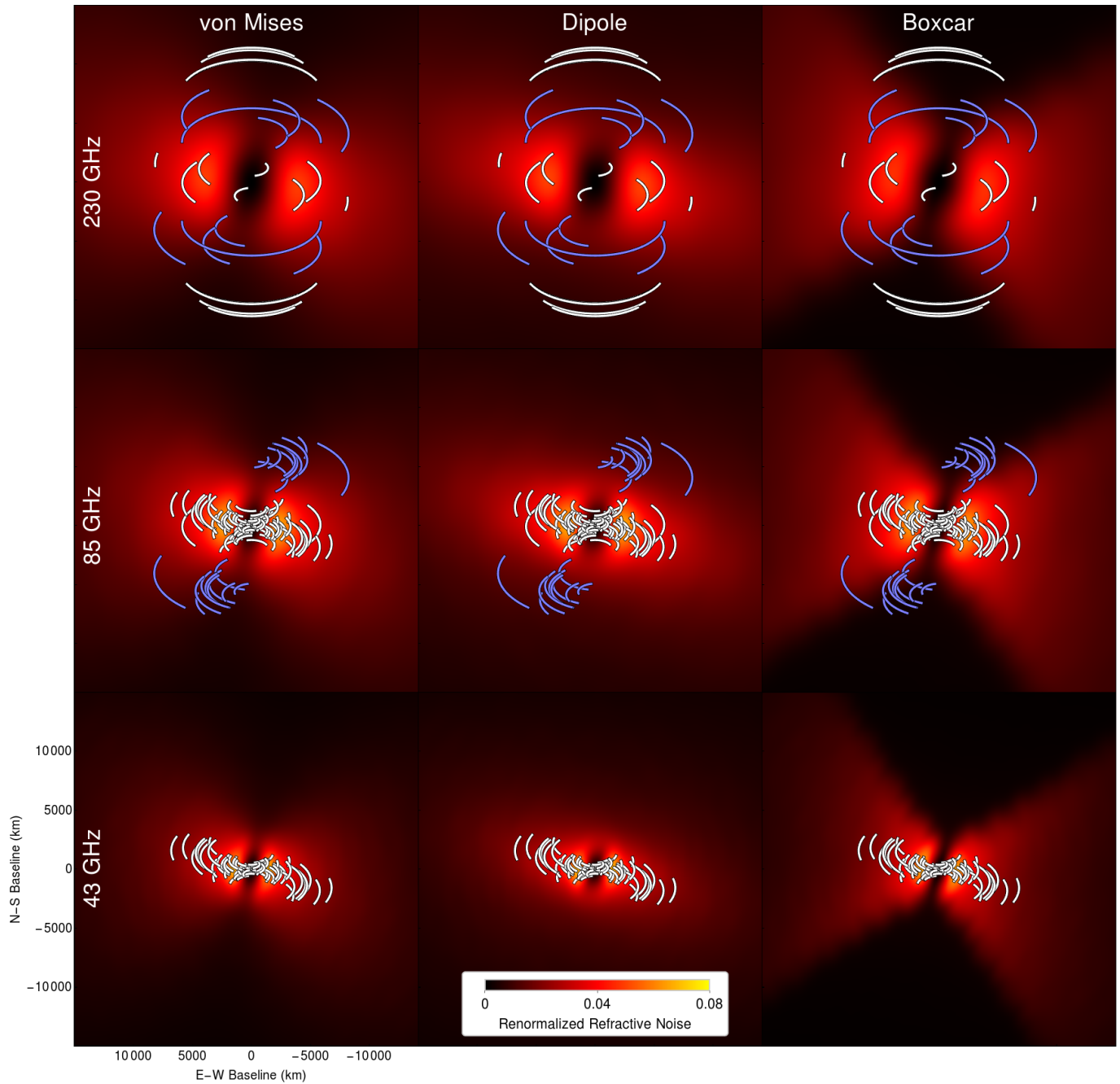


Figure 13. The standard deviation of the renormalized refractive noise (i.e., removing contributions from flux modulation and image wander and expressed as a fraction of the total flux density) as a function of the interferometric baseline. Scattering and source parameters are appropriate for Sgr A* (see text for details). Three scattering models are shown for three standard observing frequencies: 230 GHz (the EHT), 85 GHz (the GMVA), and 43 GHz (the VLBA). White tracks show baseline coverage for each array; blue tracks show baselines to ALMA.

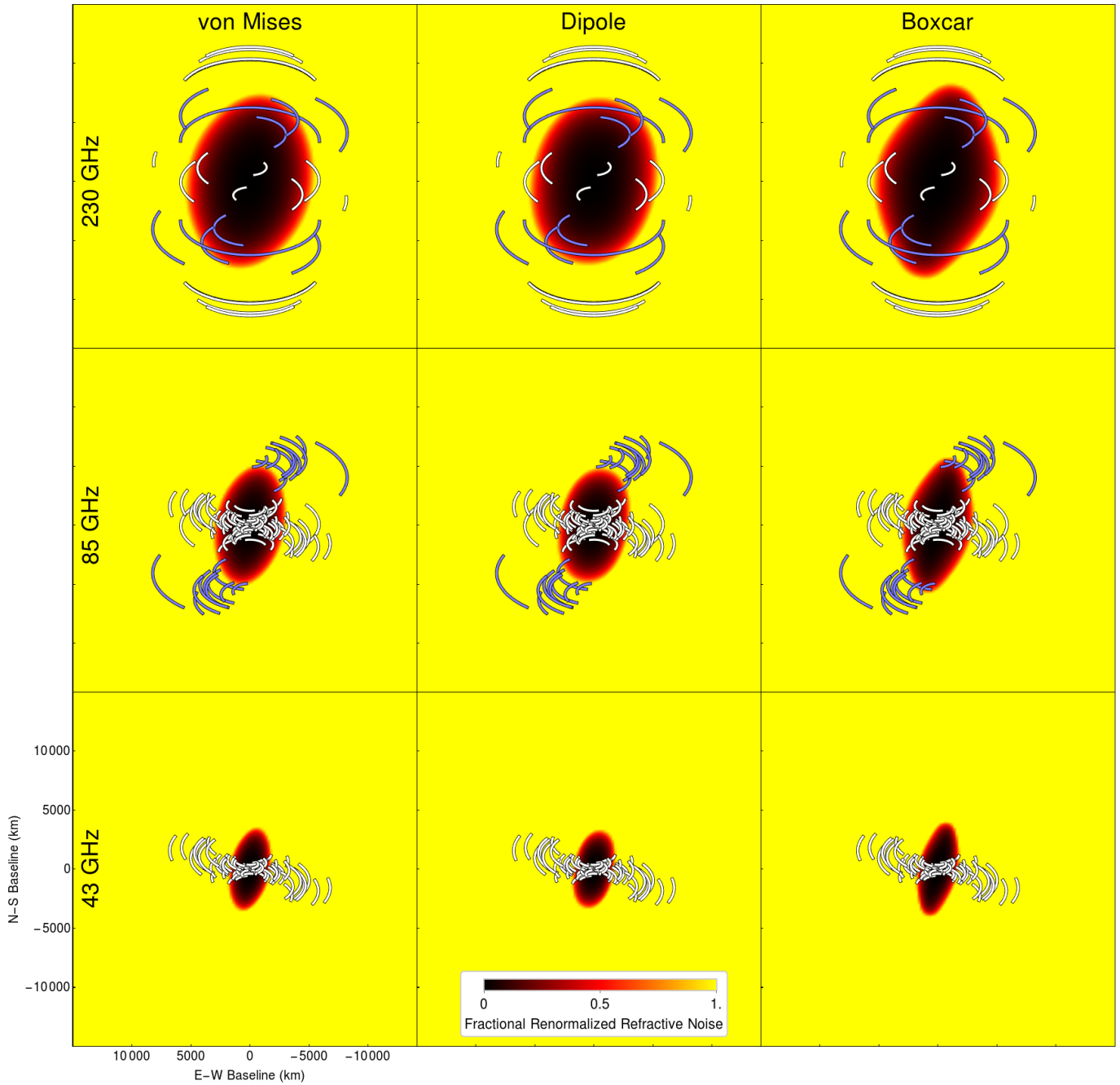


Figure 14. Same as Figure 13 but showing the renormalized refractive noise on each baseline as a fraction of the ensemble-average visibility on that baseline. Hence, on baselines for which this value is comparable to or greater than unity, measured interferometric visibilities will be dominated by random fluctuations from refractive scattering rather than from intrinsic structure for this Gaussian source model.

dominance of refractive to signal power on each baseline. In these cases, where the unscattered source is a Gaussian, the refractive noise is dominant for most long baselines at each frequency (e.g., all baselines to ALMA are dominated by refractive noise at 3 mm). However, if the intrinsic source has substructure, then the ensemble-average visibility on long baselines will be higher, decreasing the relative influence of refractive noise on those baselines.

7. CONCLUSIONS

In this paper, we developed a model of anisotropic interstellar scattering towards Sgr A* that allows us to extrapolate the properties of the scattering screen, as measured at longer wavelengths, down to the mm wavelengths at which the Event Horizon Telescope will operate when observing Sgr A*. At these short wavelengths, the diffractive scale in the scattering screen is likely to become comparable to or smaller than the inner scale of turbulence, and this will result in a number of effects:

- (i) The scattering kernel will evolve from an anisotropic Gaussian to an anisotropic exponential with a different logarithmic dependence on baseline length.
- (ii) The orientation of anisotropy in the scattering kernel, i.e., the position angle in the sky of the major axis of the scattering kernel, will not change.
- (iii) The degree of anisotropy, i.e., the ratio of the major to the minor axis, will increase with decreasing wavelength in a way that depends on the power-law index α of the turbulence spectrum and on the inner scale r_{in} of the spectrum of turbulence.
- (iv) The properties of the scattering kernel — the scatter broadened ensemble average image of a point source — will depend only weakly on the detailed angular dependence of the power spectrum of density fluctuations in the scattering screen.

(v) In contrast, the rms refractive visibilities at baseline lengths larger than the diffractive scale will depend very strongly on the angular dependence of the power spectrum of density fluctuations. In some models, the power could be negligibly small at orientations perpendicular to the major axis of the scattering kernel.

(vi) Given the expected intrinsic size of Sgr A*, refractive distortions of the scatter broadened image will be potentially detectable at wavelengths $\lambda \gtrsim 1$ mm, but will be weak at shorter wavelengths.

Some (but not all) of the above results have been recognized in previous work, though this is the first time these predictions have been collected together in the context of the EHT. In a forthcoming article, we will use archival, high-resolution, long wavelength observations of Sgr A* to infer the model parameters for the scattering screen towards this source, and use the model to make more detailed predictions of the effects of interstellar scattering on imaging observations with the EHT.

This was partially supported by NASA TCAN awards NNX14AB48G and NNX14AB47G as well as by NSF grants AST-1312034, AST-1312651, AST-1440254, and AST-1614868. We also thank the Gordon and Betty Moore Foundation (GBMF-5278) for financial support of this work. DP acknowledges support from the Radcliffe Institute for Advanced Study at Harvard University. L.M. was supported by NFS GRFP grant DGE 1144085. This work was also supported in part by the Black Hole Initiative at Harvard University, which is supported by a grant from the John Templeton Foundation. DP and LM thank the Black Hole Initiative for their hospitality.

APPENDIX

A. PARAMETERS OF APPROXIMATE EXPRESSIONS FOR MODEL COEFFICIENTS

Tables (2)-(3) report the coefficients of the various Padé approximations for the three parameters ζ_0 , \mathcal{B}_{maj} , and \mathcal{B}_{min} of the von Mises, the dipole, and the boxcar models.

REFERENCES

- Armstrong, J. W., Cordes, J. M., & Rickett, B. J. 1981, *Nature*, 291, 561
- Armstrong, J. W., Rickett, B. J., & Spangler, S. R. 1995, *ApJ*, 443, 209
- Bardeen, J. M. 1973, in *Black Holes (Les Astres Occlus)*, ed. C. Dewitt & B. S. Dewitt, 215
- Blandford, R., & Narayan, R. 1985, *MNRAS*, 213, 591
- Bower, G. C., Falcke, H., Herrnstein, R. M., et al. 2004, *Science*, 304, 704
- Bower, G. C., Goss, W. M., Falcke, H., Backer, D. C., & Lithwick, Y. 2006, *ApJL*, 648, L127
- Bower, G. C., Deller, A., Demorest, P., et al. 2014a, *ApJL*, 780, L2
- Bower, G. C., Markoff, S., Brunthaler, A., et al. 2014b, *ApJ*, 790, 1
- Broderick, A. E., Fish, V. L., Doeleman, S. S., & Loeb, A. 2009, *ApJ*, 697, 45
- Chael, A. A., Johnson, M. D., Narayan, R., et al. 2016, *ApJ*, 829, 11
- Chandran, B. D. G., & Backer, D. C. 2002, *ApJ*, 576, 176
- Cohen, M. H., & Cronyn, W. M. 1974, *ApJ*, 192, 193
- Coles, W. A., Rickett, B. J., Codona, J. L., & Frehlich, R. G. 1987, *ApJ*, 315, 666
- Cronyn, W. M. 1972, *ApJ*, 174, 181

Table 2. Parameters for the Padé approximations for the degree of anisotropy ζ_0

Parameters	von Mises Model	Dipole Model	Boxcar Model
$\zeta_{u,0}$	0	0	0
$\zeta_{u,1}$	0	$2+\alpha$	1
$\zeta_{u,2}$	0.125	$3(1+\alpha/2)$	4
$\zeta_{u,3}$	0	$(320+164\alpha+4\alpha^2+\alpha^3)/256$	4.69
$\zeta_{u,4}$	0.00595	$(64+36\alpha+4\alpha^2+\alpha^3)/512$	1.38
$\zeta_{u,5}$	0	0	0
$\zeta_{u,6}$	0.0000465	0	0
$\zeta_{d,0}$	1	8	1
$\zeta_{d,1}$	0	16	4
$\zeta_{d,2}$	0.214	$3(112+2\alpha+\alpha^2)/32$	6.34
$\zeta_{d,3}$	0	$(80+6\alpha+3\alpha^2)/32$	4.67
$\zeta_{d,4}$	0.00744	$(1920+464\alpha+236\alpha^2+4\alpha^3+\alpha^4)/12288$	1.39
$\zeta_{d,5}$	0	0	0
$\zeta_{d,6}$	0.0000496	0	0

- Dexter, J., Agol, E., & Fragile, P. C. 2009, *ApJL*, 703, L142
- Dexter, J., Agol, E., Fragile, P. C., & McKinney, J. C. 2010, *ApJ*, 717, 1092
- Dexter, J., Deller, A., Bower, G. C., et al. 2017, *MNRAS*, 471, 3563
- Doeleman, S. S., Shen, Z.-Q., Rogers, A. E. E., et al. 2001, *AJ*, 121, 2610
- Doeleman, S. S., Weintroub, J., Rogers, A. E. E., et al. 2008, *Nature*, 455, 78
- Falcke, H., Melia, F., & Agol, E. 2000, *ApJL*, 528, L13
- Fish, V. L., Doeleman, S. S., Beaudoin, C., et al. 2011, *ApJL*, 727, L36
- Fish, V. L., Johnson, M. D., Lu, R.-S., et al. 2014, *ApJ*, 795, 134
- Fish, V. L., Johnson, M. D., Doeleman, S. S., et al. 2016, *ApJ*, 820, 90
- Frail, D. A., Diamond, P. J., Cordes, J. M., & van Langevelde, H. J. 1994, *ApJL*, 427, L43
- Goldreich, P., & Sridhar, S. 1995, *ApJ*, 438, 763
- . 1997, *ApJ*, 485, 680
- Goodman, J., & Narayan, R. 1985, *MNRAS*, 214, 519
- . 1989, *MNRAS*, 238, 995
- Gwinn, C. R., Kovalev, Y. Y., Johnson, M. D., & Soglasnov, V. A. 2014, *ApJL*, 794, L14
- Johnson, M. D. 2016, *ApJ*, 833, 74
- Johnson, M. D., & Gwinn, C. R. 2015, *ApJ*, 805, 180
- Johnson, M. D., & Narayan, R. 2016, *ApJ*, 826, 170
- Johnson, M. D., Fish, V. L., Doeleman, S. S., et al. 2015, *Science*, 350, 1242
- Kim, J., Marrone, D. P., Chan, C.-K., et al. 2016, *ApJ*, 832, 156
- Krichbaum, T. P., Graham, D. A., Witzel, A., et al. 1998, *A&A*, 335, L106
- Lazio, T. J. W., & Cordes, J. M. 1998a, *ApJS*, 118, 201
- . 1998b, *ApJ*, 505, 715
- Lee, L. C., & Jorjipii, J. R. 1975a, *ApJ*, 196, 695
- . 1975b, *ApJ*, 201, 532
- . 1975c, *ApJ*, 202, 439
- Lo, K. Y., Backer, D. C., Kellermann, K. I., et al. 1993, *Nature*, 362, 38
- Lo, K. Y., Shen, Z.-Q., Zhao, J.-H., & Ho, P. T. P. 1998, *ApJL*, 508, L61
- Lu, R.-S., Krichbaum, T. P., Eckart, A., et al. 2011, *A&A*, 525, A76
- Luminet, J.-P. 1979, *A&A*, 75, 228
- Mardia, K., & Jupp, P. 1999
- Mościbrodzka, M., Falcke, H., Shiokawa, H., & Gammie, C. F. 2014, *A&A*, 570, A7
- Mościbrodzka, M., Gammie, C. F., Dolence, J. C., Shiokawa, H., & Leung, P. K. 2009, *ApJ*, 706, 497
- Narayan, R. 1992, *Philosophical Transactions of the Royal Society of London Series A*, 341, 151
- Narayan, R., & Goodman, J. 1989, *MNRAS*, 238, 963
- Narayan, R., & Hubbard, W. B. 1988, *ApJ*, 325, 503

Table 3. Parameters for the Padé approximations for the quantity \mathcal{B}_{maj}

Parameters	von Mises Model	Dipole Model	Boxcar Model
$\mathcal{B}_{u,0}$	1	1	1
$\mathcal{B}_{u,1}$	0	2.26	5.25
$\mathcal{B}_{u,2}$	0.321	1.74	11.64
$\mathcal{B}_{u,3}$	0	0.520	11.20
$\mathcal{B}_{u,4}$	0.01211	0.0467	4.199
$\mathcal{B}_{u,5}$	0	0	0
$\mathcal{B}_{u,6}$	0.0000795	0	0
$\mathcal{B}_{d,0}$	1	1	1
$\mathcal{B}_{d,1}$	0	2.32	5.23
$\mathcal{B}_{d,2}$	0.339	1.84	11.99
$\mathcal{B}_{d,3}$	0	0.564	12.47
$\mathcal{B}_{d,4}$	0.01315	0.0519	4.672
$\mathcal{B}_{d,5}$	0	0	0
$\mathcal{B}_{d,6}$	0.0000878	0	0

Ortiz-León, G. N., Johnson, M. D., Doeleman, S. S., et al. 2016,

[ApJ, 824, 40](#)

Özel, F., Psaltis, D., & Narayan, R. 2000, [ApJ, 541, 234](#)

Psaltis, D., Özel, F., Chan, C.-K., & Marrone, D. P. 2015, [ApJ, 814, 115](#)

Rickett, B., Johnston, S., Tomlinson, T., & Reynolds, J. 2009,

[MNRAS, 395, 1391](#)

Rickett, B. J. 1990, [ARA&A, 28, 561](#)

Shen, Z.-Q., Lo, K. Y., Liang, M.-C., Ho, P. T. P., & Zhao, J.-H. 2005, [Nature, 438, 62](#)

Spangler, S. R., & Gwinn, C. R. 1990, [ApJL, 353, L29](#)

Spitler, L. G., Lee, K. J., Eatough, R. P., et al. 2014, [ApJL, 780, L3](#)

van Langevelde, H. J., Frail, D. A., Cordes, J. M., & Diamond, P. J. 1992, [ApJ, 396, 686](#)

Table 4. Parameters for the Padé approximations for the quantity \mathcal{B}_{\min}

Parameters	von Mises Model	Dipole Model	Boxcar Model
$\mathcal{M}_{u,0}$	1	1	1
$\mathcal{M}_{u,1}$	0	1.738	2.486
$\mathcal{M}_{u,2}$	0.109	0.9567	2.254
$\mathcal{M}_{u,3}$	0	0.1795	0.7255
$\mathcal{M}_{u,4}$	0.00234	0.007659	0.0508
$\mathcal{M}_{u,5}$	0	0	0
$\mathcal{M}_{u,6}$	9.307×10^{-6}	0	0
$\mathcal{M}_{d,0}$	1	1	1
$\mathcal{M}_{d,1}$	0	1.6755	2.288
$\mathcal{M}_{d,2}$	0.0913	0.8676	1.585
$\mathcal{M}_{d,3}$	0	0.1445	0.2821
$\mathcal{M}_{d,4}$	0.00165	0.004417	0.00565
$\mathcal{M}_{d,5}$	0	0	0
$\mathcal{M}_{d,6}$	5.067×10^{-6}	0	0